Advanced Robotics Research

WILEY VCH

ADVANCED ROBOTICS RESEARCH Open Access

REVIEW OPEN ACCESS

Waveguide Photoactuators: Materials, Fabrication, and Applications

Minjie Xi[1,2,3] | Hemin Pan[1,2,3] | Yang Zong[1,2,3] | Yongfeng Mei[1,2,3,4] | Jizhai Cui[1,2,3]

[1]International Institute for Intelligent Nanorobots and Nanosystems & State Key Laboratory of Surface Physics, College of Intelligent Robotics and Advanced Manufacturing, Fudan University, Shanghai, China | [2]Yiwu Research Institute of Fudan University, Yiwu, China | [3]Shanghai Key Laboratory of Metasurfaces for Light Manipulation, Fudan University, Shanghai, China | [4]Shanghai Frontiers Science Research Base of Intelligent Optoelectronics and Perception, Institute of Optoelectronics, Fudan University, Shanghai, China

Correspondence: Jizhai Cui (jzcui@fudan.edu.cn)

Received: 5 August 2025 | **Revised:** 29 September 2025

Funding: National Key Technologies R&D Program of China, Grant/Award Numbers: 2022YFA1207000 2022YFA1404700 2021YFA0715302; National Natural Science Foundation of China, Grant/Award Numbers: 52101214 62375054; Shanghai Rising-Star Program, Grant/Award Number: 24QA2700700; Science and Technology Commission of Shanghai Municipality, Grant/Award Numbers: 24520750200 24CL2900200; Shanghai Talent Programs

Keywords: micro-manipulation | optical fiber | photoresponsive materials | waveguide photoactuator

ABSTRACT

Waveguide photoactuators direct light through optical fibers or planar waveguides to stimuli-responsive materials, converting optical energy into precise mechanical motion without the alignment constraints or undesired scattering of free-space illumination. Their tethered yet flexible architecture promises applications in minimally invasive surgical tools, soft robotic grippers for confined spaces, and reconfigurable elements for integrated photonic circuits. This review contrasts the major actuation pathways, namely photothermal, photochemical, and optical-force mechanisms, and identifies representative material platforms that enable them. It then surveys principal waveguide geometries and summarizes fabrication and integration approaches that join waveguides with active films while maintaining optical coupling efficiency and mechanical robustness. Deformation concepts are organized around stress-mismatch bilayers and asymmetric illumination, which provide a unified account of bending, hooking, coiling, and pumping behaviors. A comparative performance analysis highlights thickness reduction, interface durability, and liquid-phase operation as key levers for future improvement, and outlines how programmable alignment or patterned inert layers can further expand functionality. By connecting these elements into a coherent framework, the review aims to guide materials selection, device design, and system integration, accelerating the transition of waveguide photoactuators from laboratory prototypes to versatile microscale tools for complex real-world environments.

1 | Introduction

Actuators that transduce external stimuli into mechanical work constitute the foundation of numerous micro- and macroscale systems. By converting absorbed energy into internal stress and strain [1], they produce deformation modes ranging from contraction [2, 3], expansion [4, 5], and bending [6–8] to twisting and complex multimodal motions [9, 10]. The external stimuli includes thermal fields [11], electrical potentials [12–14], magnetic flux [15, 16], chemical gradients [17, 18], humidity [19, 20], and—of particular relevance here—light [21, 22]. Light-driven actuation offers several distinctive advantages. First, optical energy can be delivered at high speed, outperforming diffusion-limited triggers such as heat or moisture. Second, optical control dispenses with complex wiring, enabling wireless operation in confined or mobile platforms. Third, the tunability of wavelength, intensity, and polarization provides submicron spatial addressability and temporal on–off gating, thus

permitting programmable motion patterns that are difficult to replicate with alternative stimuli [1, 21–24]. In addition, light sources are easily modulated, inherently clean, and compatible with remote or in vivo environments, and can act either through direct photothermal conversion [25–27] or photochemical processes [28, 29], further enriching the design space. These light-driven actuations have been implemented in a broad range of responsive media, including carbon-based nanocomposites [24], hydrogels [30], liquid-crystal polymers [31], and shape-memory polymers [32], each offering distinct advantages in response speed, strain amplitude, and environmental compatibility. Nevertheless, regardless of the internal conversion mechanism, the macroscopic effectiveness of a photoactuator ultimately depends on how efficiently photons are delivered from the light source to the responsive medium.

Most reported photoactuators rely on externally applied, or free-space illumination, whereby light is transported through air or liquid to the responsive element [33]. Although this strategy is conceptually simple, it imposes two fundamental constraints: (i) diffuse illumination distributes energy over a large solid angle, leading to low conversion efficiency [34] and (ii) tightly focused beams require active beam tracking once the actuator moves, reducing system robustness and geometric freedom [35]. Embedding the optical pathway inside a waveguide provides an elegant solution. Optical waveguides deliver photons through total internal reflection with minimal loss, decoupling energy transport from the surrounding medium and the actuator's own motion. Consequently, waveguide-integrated photoactuators combine the precision of directional irradiation with the flexibility of wireless operation, making them attractive for soft robotics, biomedical tools, and reconfigurable devices functioning in opaque or confined environments [36–39].

This review presents a survey of the recent advances of waveguide photoactuators. We first classify the photoreactive materials and waveguide architectures employed, along with the underlying photothermal and photochemical mechanisms. We then discuss fabrication and integration strategies that couple waveguides to active elements, highlighting how structural design dictates deformation behavior. Performance metrics across material platforms are compared to elucidate current trade-offs, followed by an overview of demonstrated applications (Figure 1). Finally, we outline pressing challenges and promising research directions that will guide the next phase of development.

2 | Photoresponsive Materials and Optical Waveguide

2.1 | Photoresponsive Materials

The photoresponsive material is the core component that converts optical energy into mechanical motion in a waveguide-based actuator. Three mechanisms are involved: the photothermal effect, photochemical effects, and optical forces (Figure 2) [21]. Specifically, the photothermal effect converts optical energy into heat, inducing thermal expansion/contraction or phase transitions in the material; the photochemical effects involve reversible structural changes in photosensitive molecules within the material triggered by light; while optical forces directly transduce the radiation pressure of light into mechanical energy.

2.1.1 | Photothermal Actuation

Photothermal actuation requires a material that can both efficiently absorb light and convert the resulting temperature change into deformation. Thermally responsive materials include liquid crystal elastomers (LCEs) [46], hydrogels [47], and shape-memory polymers (SMPs) [32] and polymers with a high coefficient of thermal expansion [36]. Photothermal conversion is

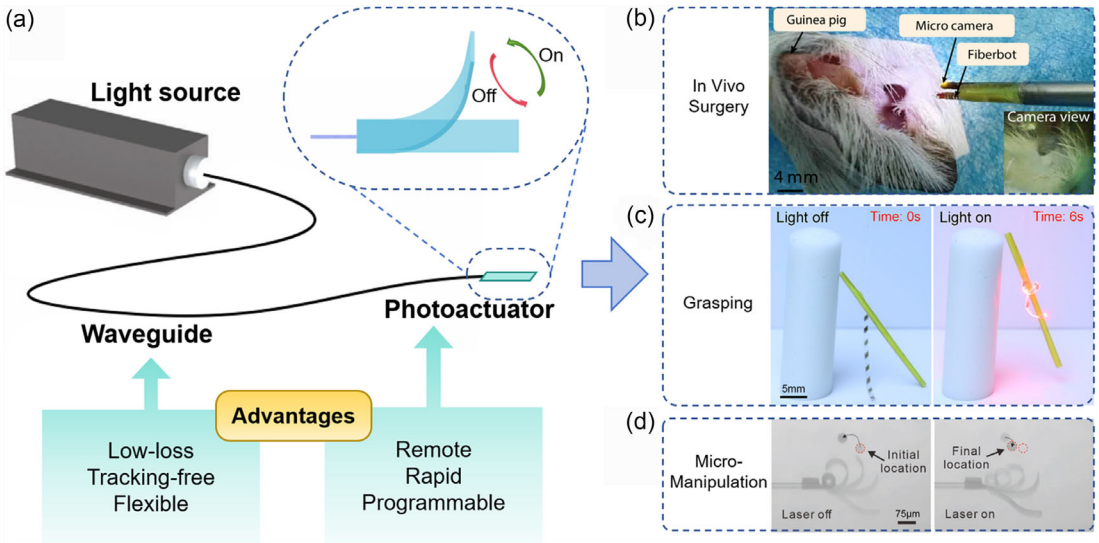

FIGURE 1 | Schematic and applications of waveguide photoactuator. (a) Schematic of the system. (b) Applications for in vivo surgery. Reproduced with permission [37]. Copyright 2024, The American Association for the Advancement of Science (AAAS). (c) Applications for grasping. Reproduced with permission [36]. Copyright 2025, John Wiley and Sons (Wiley). (d) Applications for micromanipulation. Reproduced with permission [38]. Copyright 2025, Wiley.

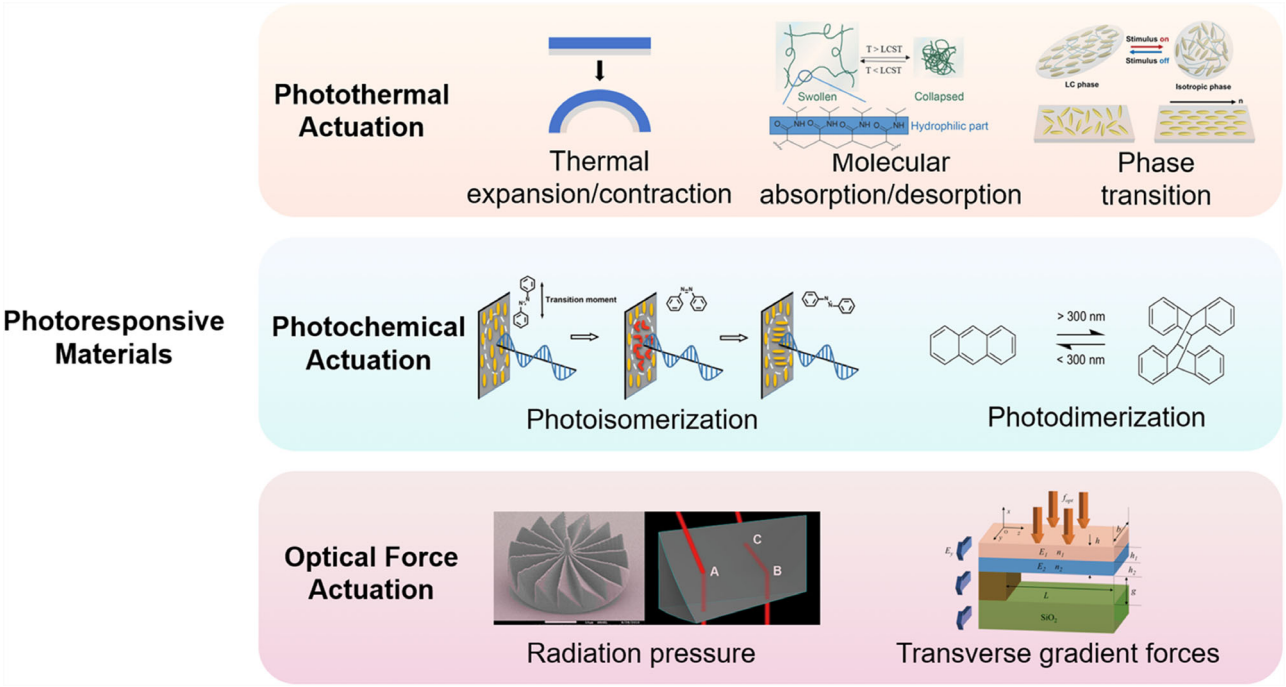

FIGURE 2 | Three types of photoresponsive materials: photothermal actuation, photochemical actuation and optical force actuation [40–45]. Top panel: thermal expansion/contraction, molecular absorption/desorption, and phase transition. Reproduced with permission [40, 41]. Left second to right: Copyright 2018, Wiley; Copyright 2022, AIP Publishing. Middle panel: photoisomerization and photodimerization. Reproduced with permission or under the terms of the CC-BY license [42, 43]. Left to right: Copyright 2019, Wiley; Copyright 2022, Springer Nature. Bottom panel: radiation pressure and transverse gradient forces. Reproduced with permission [44, 45]. Left to right: Copyright 2012, AIP Publishing; Copyright 2022, Elsevier.

often enhanced by dispersing carbon-based nanomaterials [48], noble metal nanostructures such as Au and Ag [49], or transition-metal sulfide [50] and oxide nanoparticles [51]. In some cases, the host polymer itself absorbs light strongly enough to act without additives, whereas in others, a composite design is adopted wherein light is first converted to heat and the heat then drives shape change.

A single homogeneous layer rarely produces a large displacement because its thermal expansion is limited by its own coefficient of thermal expansion (CTE). To overcome this limitation, multilayer films with mismatched CTEs are employed, generating interfacial stresses that bend the stack under illumination [38]. Polydimethylsiloxane (PDMS) is widely used as one of the multilayers in optical waveguide-based actuators due to its high CTE (3×10^{-4} K^{-1}), exceptional flexibility, optical transparency, and ease of manufacturing [25].

In addition to simple photothermal expansion, the photothermal effect can also induce molecular absorption or desorption, leading to significant volume changes. Polymeric hydrogels represent a class of widely utilized photothermal materials characterized by cross-linked hydrophilic networks with high water content [30]. A representative thermoresponsive hydrogel is poly(N-isopropylacrylamide) (PNIPAM) [52]. Its polymer chains contain amide and isopropyl moieties, which confer a lower critical solution temperature (LCST, ≈32°C) in aqueous media [53]. Below the LCST, PNIPAM maintains a hydrated state through hydrogen bonding between its amide groups and water molecules, resulting in an entropically stable, expanded coil conformation that keeps the polymer swollen. Above the LCST, hydrogen bonds weaken while hydrophobic interactions between isopropyl groups dominate. The resulting entropy gain from water molecule release drives dehydration and chain collapse, causing PNIPAM to transition into compact globules through an entropy-driven phase separation process [30]. This unique property of PNIPAM makes it well-suited as a photothermal-responsive material for waveguide photoactuators requiring high deformability.

Phase-transition-driven polymers form another important family of photothermal actuators, with SMPs and LCEs being two prominent examples. Both systems store elastic energy through an internal order–disorder transition and release it as mechanical work when the phase state reverses. SMPs are polymers that can be fixed in a temporary shape and can recover their permanent shape upon exposure to an external stimulus such as heat. Generally, SMPs are deformed at a deformation temperature (T_d), and the deformed temporary shape is fixed upon cooling. When heated to a recovery temperature (T_r), the permanent shape is recovered [21]. Common types of SMPs include polyurethane [54], polystyrene [55], polyethylene [56], and epoxy [57]. Photothermal actuation is enabled by incorporating SMPs with light-heat conversion materials [58]. For conventional SMPs with unidirectional shape memory effects, reprogramming the permanent shape requires external force to first establish a new temporary shape [32]. Therefore, unidirectional SMPs are unsuitable for repeated cyclic operation under light-driven conditions alone. LCEs consist of cross-linked polymer chains that incorporate liquid crystal mesogens, whose orientation dictates the mechanical properties of the bulk material [59]. The combination of the self-organizing LC networks and the flexible rubber

network allows for large and reversible anisotropic dimensional changes in response to applied stimuli. LCEs are characterized by low cross-linking density, flexible polymer backbones, relatively fast stimuli-response (≈100 ms) [60], large anisotropic and local deformations (up to 500% strain) [61], and soft elasticity [62] (i.e., nonlinear response to mechanical force). The molecular orientation of LCEs can be precisely controlled, enabling tailored alignment in local network domains to program both magnitude and direction of mechanical strain responses [41].

The discussion above has focused on the three photothermal response mechanisms—thermal expansion, molecular adsorption/desorption, and phase transition—by highlighting materials currently utilized in optical waveguide-based actuators. Beyond these, numerous other photothermally responsive materials employed in conventional photoactuators demonstrate potential for waveguide-integrated applications. For instance, viable thermal expansion materials include polyimide (PI) [63], polycarbonate (PC) [64], biaxially oriented polypropylene (BOPP) [65], poly(vinylidene fluoride) (PVDF) [66], and polyethylene (PE) [67]. In the category of molecular adsorption/desorption materials, graphene oxide (GO) [68] and polydopamine (PDA) [26] can also release water upon photothermal stimulation. Additionally, photothermal phase-change materials for actuators include vanadium dioxide (VO_2) [27]. These materials represent promising candidates awaiting full exploitation in integrated waveguide platforms.

2.1.2 | Photochemical Actuation

Photochemical actuation relies on reversible light-induced reactions that occur with minimal temperature change. These photochemical reactions include photoisomerization and photodimerization. Photoisomerization includes trans-cis isomerization, keto-enol tautomerism, and ring-opening and closure, whereas photodimerization comprises [2 + 2] and [4 + 4] cycloadditions [22].

Azobenzene (Azo) derivatives are the primary photochemical materials used in waveguide photoactuators, relying on reversible trans-cis photoisomerization. The azobenzene molecule, which consists of two phenyl rings linked by an azo (-N═N-) bond, is a reversible light-switchable compound that undergoes photoisomerization [69, 70]. When the Azo film is irradiated by UV light, trans-cis isomerization of Azo occurs, disrupting the molecular order and resulting in mechanical deformation. Under visible light irradiation, the cis form of Azo isomerize changes to the trans form and the film returns to its original shape [71, 72].

Other photochemically responsive materials have also been utilized in photoactuators. Keto-enol tautomerism is another photoisomerization mechanism, where light triggers an intramolecular proton transfer, switching the molecule between its keto and enol forms and resulting in macroscopic deformation. A prominent example is salicylideneaniline crystals, which bend by 45° under UV light and recover their original state under visible light [73]. Another major photoisomerization mechanism involves ring-opening and closure, as seen in materials such as diarylethenes [74] and spiropyran derivatives [75]. In these systems, UV light induces ring closure, altering the molecule's shape and properties, while visible light triggers the ring-opening reaction.

Furthermore, photodimerization achieves actuation through light-induced cycloaddition reactions, in which two molecules form a new bond, generating significant internal strain within a material. Specifically, UV light triggers [2 + 2] or [4 + 4] cycloaddition reactions between adjacent molecules, which drastically alters their geometry and accumulating strain within the crystal lattice. For instance, crystals undergoing [2 + 2] cycloaddition, such as certain Zn-complexes, can exhibit dramatic motions including popping, rolling, flipping, and jumping, driven by the resulting strain [29]. Anthracene derivatives, conversely, undergo [4 + 4] cycloaddition reactions [76]. These photodimerization reactions offer a purely optical control scheme for actuation and have the significant advantage of eliminating thermal crosstalk with the environment.

2.1.3 | Optical Force Actuation

When a focused laser beam irradiates an object, optical forces arise from the exchange of momentum between light and matter, as required by the law of conservation of momentum [77, 78]. Optical forces are generally divided into two major categories: radiation pressure and transverse gradient forces. Radiation pressure acts along the light propagation direction. One of its key applications is the self-cooling of micromechanical resonators, achieved by using a red-detuned laser to induce dynamic back-action and viscous damping [79]. It can also directly drive mechanical motion, as demonstrated by the efficient rotation of turbine-like micro-rotors through photon momentum transfer [44]. Furthermore, radiation pressure enables ultra-long-range optical pulling of microdroplets along a subwavelength optical nanofiber via engineered Minkowski momentum, achieving pulling distances up to 40 cm and even vertical motion against gravity [80]. Transverse gradient force acts transversely to the propagation direction of light and has been widely used to trap and manipulate small particles in optical tweezers setups [81]. Furthermore, this gradient force also enables displacement of integrated nanophotonic structures. Evanescent coupling in waveguides significantly amplifies gradient optical forces by intensified field gradients. For example, optical-force-driven mechanical motion between a suspended Si waveguide and silica substrate has been experimentally demonstrated [82]. Similarly, evanescently coupled waveguides can enhance gradient optical forces by orders of magnitude due to the resulting intensified optical field gradients [83]. However, because optical forces are weak, they are mainly useful at the sub-hundred-micrometer scale, whereas photothermal and photochemical mechanisms dominate larger devices.

2.2 | Optical Waveguides

An optical waveguide is a dielectric structure that confines and guides light propagation. These waveguides are categorized into two primary classes: cylindrical waveguides, commonly known as optical fibers, and integrated optical waveguides—including planar (thin-film) and strip-type dielectric configurations—which are critical components within optoelectronic integrated devices or systems. Fundamentally, an optical waveguide is a

transparent dielectric structure (e.g., silica glass) that transmits optical-frequency electromagnetic waves. Its waveguiding mechanism fundamentally differs from metallic enclosed waveguides: Total internal reflection at interfaces between media of differing refractive indices confines light propagation within and near the waveguide structure. Both multimode and single-mode optical fibers have been successfully deployed in telecommunications. For light-driven actuators, utilizing optical waveguides as light transmission pathways offers several key advantages: overcoming environmental constraints on free-space light propagation, enabling long-distance transmission with minimal propagation losses, achieving precise spatial control of light delivery, and providing programmable optical attenuation capabilities [33].

2.2.1 | Optical Fibers

An optical fiber is a cylindrical dielectric waveguide that transmits light via total internal reflection, comprising three structural layers: the core, cladding, and coating (Figure 3a). The core's higher refractive index relative to the cladding enables light propagation through continuous total internal reflection. Functionally, optical fibers efficiently transmit data, images, or energy as light pulses, serving as fundamental components in modern telecommunications, medical technologies, and sensing systems by efficiently transmitting data or power in the form of light pulses [84–86]. Within optical waveguide-based actuators, fibers represent the most prevalent waveguide form. They can be classified by material into silica fibers and polymer optical fibers (POF), and by fabrication method into commercially standardized fibers, custom-synthesized waveguide fibers, and taper-processed microfibers.

Silica fibers, fabricated from silicon dioxide, are extensively utilized in telecommunications and sensing applications [87]. Based on transmission mode, they are divided into single-mode fibers (SMF) and multimode fibers (MMF) (Figure 3b). SMFs feature ultrathin cores (typically 8–10 μm diameter) with step-index profiles that permit only fundamental mode propagation, and therefore exhibit high susceptibility to bending. SMFs operate primarily in the near-infrared spectrum. Conversely, MMFs possess larger cores (typically 50–62.5 μm diameter), often with graded-index profiles to support hundreds of propagation modes. MMFs operate predominantly at shorter wavelengths and demonstrate enhanced flexibility due to their robust core design. Both SMFs and MMFs are widely implemented in optical waveguide-based actuators [37, 38].

POFs utilize core materials such as polymethyl methacrylate (PMMA), polystyrene (PS), and polycarbonate (PC). Compared with conventional silica fibers, POF offers distinct advantages including exceptional mechanical flexibility, cost-effectiveness, and simplified optical coupling—making them suitable for short-distance communications, industrial controls, and consumer electronics. They typically feature large core diameters (typically 0.5–1 mm) and function primarily as step-index multimode fibers for visible light transmission. Although they exhibit higher attenuation over long distances than silica fibers, POFs provide superior resistance to bending and vibration, reduced weight, and significantly lower manufacturing costs [88–90].

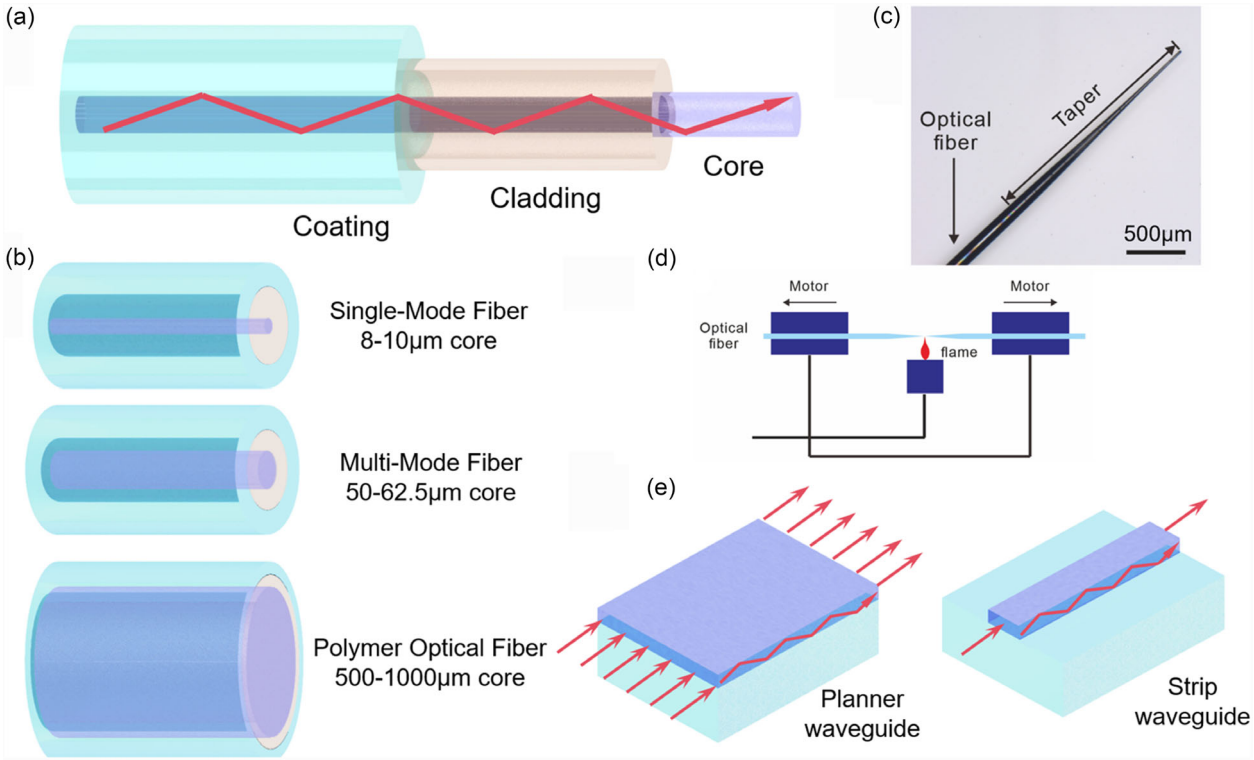

FIGURE 3 | Schematics of optical waveguides. (a) Schematic illustrating the structure of an optical fiber. (b) Schematics of silica single-mode fiber, silica multi-mode fiber and polymer optical fiber. (c) Microscope image of a tapered optical fiber. Reproduced with permission [38]. Copyright 2025, Wiley. (d) Schematic of flame-heated taper drawing process. Reproduced with permission [38]. Copyright 2025, Wiley. (e) Schematics of planner waveguide and strip waveguide.

When deploying commercial optical fibers in waveguide photoactuators, the required lengths are much shorter than in telecommunications applications. Consequently, transmission losses and costs become negligible factors. Fiber selection primarily depends on operational wavelength range and optical coupling efficiency. To enhance integration between waveguides and actuators, custom-synthesized waveguide fibers—fabricated from materials like PDMS [36, 91, 92], LCE [90], or photocurable resin [89]—are increasingly utilized. These can serve either as interfacial connectors between commercial fibers and actuators, or as complete replacements that function as standalone waveguides. For actuators requiring large deformation amplitudes, intrinsic waveguiding capability within the actuator body is essential to ensure efficient light delivery to the functional segments at its distal end [36, 93, 94].

Another common optical fiber type is the micro/nanofiber (MNF), also known as a tapered optical fiber (TOF), fabricated by tapering standard optical fibers (Figure 3c). MNFs possess excellent optical and mechanical properties, including a strong evanescent field, low optical loss, wavelength-scale diameter, a small bending radius, structural versatility, and seamless connection with standard optical fiber [95–98]. Tapered fibers offer four key advantages over standard optical fibers: (1) significantly reduced active layer thickness enabled by subwavelength-scale diameters; (2) exceptionally high energy density achieved through evanescent field confinement; (3) enhanced optical coupling efficiency via mode-field matching with micro/nanoscale photo-responsive materials [33]; (4) and tunable control over the output field distribution through engineered taper geometries [99].

Consequently, the diverse optical fiber waveguide types discussed above can be optimally selected to meet different application demands (e.g., complex transmission scenarios, light source wavelengths, and actuator configurations), allowing for tailored waveguide selection and precise control over optical transmission conditions.

2.2.2 | Integrated Optical Waveguide

Planar and strip waveguides represent types of integrated optical waveguides fabricated on planar substrates (Figure 3e), enabling complex optical functionalities with broad applications in telecommunications, sensing, and quantum technologies [100]. Planar waveguides feature a trilayered dielectric structure comprising upper/lower claddings and a core layer. The core's higher refractive index confines light propagation via total internal reflection within the thin-film plane, restricting optical modes along the thickness dimension. Strip waveguides are fabricated by selectively etching the core layer of planar waveguides to form either raised ridge structures or buried channel configurations surrounded by cladding. This design confines light within the strip's cross-sectional area, providing optical restriction in both thickness and width dimensions.

Planar and strip waveguides are primarily employed in integrated photonic devices to facilitate optical signal generation, transmission, modulation, and detection [100]. Together, these functions form the optical analog to electronics integrated circuits, known as the photonic integrated circuit (PIC) [101]. Numerous studies have developed methods to dynamically control photonic devices, i.e., to realize tunable photonics. Current on-chip tuning mechanisms can be generally classified into thermo-optic [102, 103], electro-optic [104], and mechanical methods. Mechanical tuning, achieved by mechanically moving or deforming structures, is a natural way to tune photonic devices and has many advantages over other methods, such as a small footprint and process compatibility with semiconductors fabrication [105]. The mechanical tuning of PICs can be considered a form of actuation, most commonly achieved through micro-electro-mechanical systems (MEMS). By applying external forces either piezoelectrically [106] or electrostatically [107, 108], the deformation of the mechanical structure induces stress and strain on the optical waveguides [109], thereby changing the effective refractive index of the waveguide through photoelastic [110] and moving boundary effects [111]. The actuators in PICs have been applied successfully in directional couplers [112], optical switches [113], and phase shifters [114].

Waveguide actuators using optical forces represent a promising research direction for PICs, due to their potential for application in all-optical systems [105]. Driving photonic structures with optical force has already been experimentally proven [115, 116], and some of its applications, such as in filters and routers, have also been demonstrated. *Deotare* et al. leverage the optical gradient force from pump light to mechanically deform the silicon nanobeams, which are patterned with a periodic array of air holes to form photonic crystal cavities, thereby altering their mutual spacing to tune the filter's resonant wavelength [117]. *Rosenberg* et al. utilize a "spiderweb" resonator structure composed of two stacked silica microrings. By employing the optical gradient force to induce mechanical deformation of this structure, it achieves high-speed, wide-range, and loss-free static and dynamic tuning and routing of the filter's resonant wavelength [118]. Being free from electrical parasitic couplings, mechanical oscillations driven by optical forces can reach ultra-high frequencies [105]. Moreover, on-chip integrated cavity optomechanics, which originates from the coupling between optical and mechanical degrees of freedom, represents a rapidly advancing field capable of inducing mechanical amplification or cooling through photon–phonon interactions [79]. Overall, direct light-driven operation offers distinct advantages: rapid response speeds, minimal power consumption, contactless interference immunity, and superior integration density [105, 119].

By selecting an appropriate combination of a photoresponsive material and waveguide type, designers can tailor optical delivery, mechanical stroke, and response speed to meet the requirements of various applications, ranging from precision manipulation to soft robotic locomotion.

3 | Fabrication, Integration, and Deformation Mechanisms

Waveguide photoactuators consist of an optical waveguide that transports light and a photoactuator that converts the light into motion. These two parts must operate together; however, the design requirements of one part can limit the options available for the other. The following sections describe how each part is

fabricated and integrated and then explain how the integrated system produces mechanical deformation.

3.1 | Fabrication

Three principal methods are used to form the main body of a photoactuator: mold casting, photolithographic patterning, and in situ growth on the waveguide. Mold casting offers broad applicability across various photoresponsive materials, enabling the fabrication of diverse geometries such as thin films and fibers. A common procedure involves coating a precursor solution onto a flat substrate, curing it into a thin film, and then cutting the film to the required size [39, 91, 120, 121]. Similarly, cylindrical molds can be employed to produce fiber-shaped actuators [37, 90]. SMPs can be extruded into fibers, bent using molds, and fixed, enabling them to recover their original form when heated [58]. Although straightforward, mold casting usually produces feature sizes no smaller than several tens of micrometers in thickness and millimeters in length.

The photolithographic patterning method involves sequential steps of spin-coating, UV lithography, and development. Among current photoresponsive materials, PNIPAM hydrogel is compatible with this technique, enabling the fabrication of microscale planar structures. Leveraging the exceptional precision of photolithographic patterning, actuators can be fabricated into complex planar geometries beyond conventional rectangular shapes, with thicknesses typically ranging from several to tens of micrometers [38, 89]. In situ growth on a waveguide currently lacks a standardized procedure and is therefore discussed together with integration methods in the next subsection.

Following or during the fabrication of the photoactuator's primary structure, various post-treatments can be applied to enhance photothermal conversion efficiency and mechanical actuation performance. Photothermal fillers such as noble metal nanomaterials [89, 90, 92], organic photothermal dyes [121, 122], metal complex [39, 58], and carbon-based materials [36, 91] can be incorporated into the matrix to improve light absorption efficiency. For LCEs, alignment treatments are used to impose a single molecular orientation. This can be achieved either by stretching a partly cross-linked film and finishing the cross-linking while the film is held under tension or by depositing an alignment layer such as polyimide, rubbing, or photoaligning it and curing the overlying liquid-crystal monomer [41]. Bilayer devices require an inert layer, which can be deposited by vapor deposition [38, 82], coating [36, 91, 123], or an additional photolithography step [38, 89]. Additionally, inert layers may also serve as photothermal absorber [82, 123], and their patterning allows precise control of the bending direction [36, 38].

Commercial silica fibers and POFs can serve directly as waveguides. MNFs, which are fabricated by taper drawing, offer stronger evanescent fields and lower bending radii [124–126]. The fabrication of MNFs via taper drawing involves critical processes including thermal heating (via flame, laser, or electrical sources [127]), controlled stretching [128, 129], and real-time diameter monitoring [124], as outlined in Figure 3d. The tapering parameters of an optical fiber govern the resulting taper geometries, which in turn determines the optical properties of MNFs. For instance, slow pulling rates yield a gentle taper transition with uniform energy distribution, while fast pulling rates produce a sharp tip where the energy becomes highly concentrated [99].

Custom-synthesized optical waveguide fibers are primarily fabricated using PDMS, LCE, and photocurable resin. The simplest form of waveguide is a transparent medium that allows light to propagate short distances in a straight line, which can be produced through mold casting [90] or photolithographic patterning [89]. For more advanced functionality, customized optical fibers can be fabricated by separately preparing the core and cladding layers. This approach enables controlled bending of light propagationand allows for customization of the fiber's constituent materials, including the use of photoresponsive ones. One manufacturing approach involves first forming the core via mold casting, followed by spin-coating to apply the cladding [92, 94]. Another method utilizes coaxial extrusion combined with UV curing to directly produce LCE fibers with a core-cladding structure [93]. This method can produce continuous LCE fibers exceeding 5 m in length within 18 min, demonstrating high scalability.

3.2 | Integration

Because the waveguides and photoactuators usually use distinct materials, an effective integration strategy is essential. Integration affects optical coupling, mechanical stability, environmental stability, and also constrains feasible fabrication steps. Two primary integration strategies are post-fabrication assembly and monolithic fabrication.

3.2.1 | Post-Fabrication Assembly

In post-fabrication assembly, each component is fabricated separately and then joined. This approach offers high flexibility in assembly, and adhesive bonding is the simplest method. Direct adhesive bonding provides a straightforward way to secure optical fiber waveguides to photoactuators, enabling rapid and stable physical fixation. Since the actuator is positioned at the fiber's emission facet, the adhesive applied at this optical interface must be highly transparent to minimize coupling losses. Some studies have directly bonded actuators to optical fiber facets using UV-curable adhesives (Figure 4a) [89, 121]. When the cross-sectional area of the optical fiber tip does not match that of the actuator, significant light loss can occur due to scattering at the interface [89]. A more secure attachment can be achieved by fabricating hollow grooves in the actuator, inserting an optical fiber, and subsequently filling the cavity with adhesive. Small et al. drilled a coaxial socket in the SMP rod, filled it with UV-curable epoxy, inserted an optical fiber, and cured the assembly with UV light. The extruded epoxy formed a reinforcing collar [58]. Zhou et al. integrated optical fibers into hollow LCE fibers with PDMS-filled cores serving as optical transmission media (Figure 4d) [37]. Kuenstler et al. coupled the PMMA fiber to the LCE actuator through microscopic alignment and secured the assembly on a substrate using double-sided tape [90], though sacrificing the positional adjustability. Cheng et al. attached the azo-LCP strips to the side of a multimode fiber using epoxy adhesive, extending

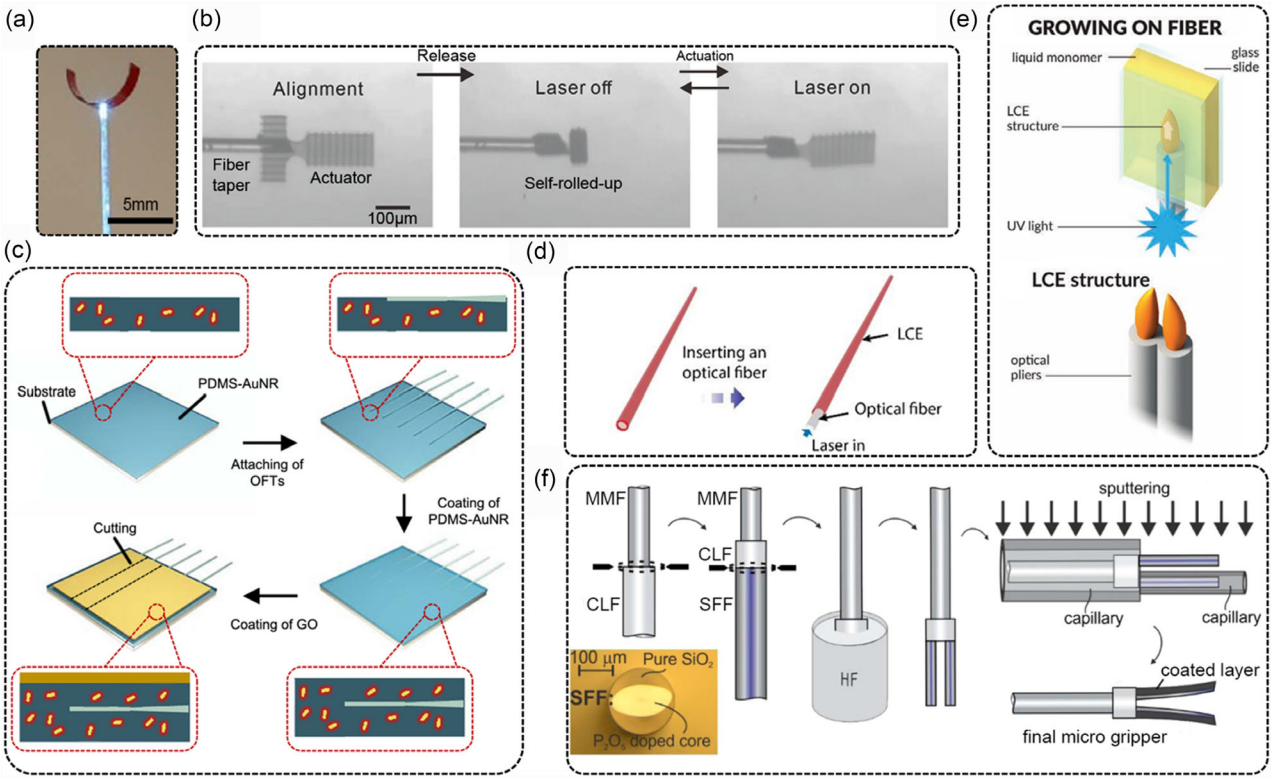

FIGURE 4 | Integration processes. (a) End-face bonding of a LCE actuator to optical fiber tip using UV adhesive. Adapted under the terms of the CC-BY license [121]. Copyright 2017, Springer Nature. (b) Utilizing the actuator's self-coiling capability to encapsulate the optical fiber tip. Adapted with permission [38]. Copyright 2025, Wiley. (c) PDMS/AuNR and GO based actuator with tapered optical fiber embedded in PDMS during fabrication. Adapted under the terms of the CC-BY license [91]. Copyright 2022, Springer Nature. (d) Plug-in coupling of a hollow LCE and an optical fiber fixed by PDMS. Reproduced with permission [37]. Copyright 2024, AAAS. (e) A LCE actuator grown in a cell filled with oriented monomer via UV light delivered through an optical fiber. Adapted with permission [122]. Copyright 2020, Wiley. (f) A leaflet-shaped fiber-blade actuator fabricated by in-situ etching of an optical fiber. Adapted with permission [123]. Copyright 2019, Optical Society of America.

the strip ends 400–500 μm beyond the fiber facet [120], which strategically minimizes adhesive-induced interference with optical coupling.

Achieving efficient optical coupling requires special attention when connecting custom-synthesized optical fibers to the commercial fibers linked to the laser source. This requires coaxial alignment of the core layers of both fibers to ensure efficient optical signal transmission [94]. Li et al. employed a precision coupling platform to ensure the end faces of the two fibers as flat as possible and in tightly contact, followed by encapsulation using UV adhesive [93]. This method achieved an optical power transmission efficiency of 63.5% for 808 nm laser transmission.

Alternatively, a self-coiling assembly approach leverages the actuator's intrinsic rolling capability. Thin-film self-rolling technology—a method utilizing internal stress gradients or external stimuli to achieve directional bending—finds broad application in micro/nano devices [130]. Zong et al. programmed self-rolling film structures to simultaneously fabricate actuators and create connector ends that coil around tapered optical fibers, establishing robust mechanical coupling without adhesives (Figure 4b) [38]. Within 1000 actuation cycles, the connection between the fiber taper and microactuator remains stable without any visible slippage or damage.

Overall, the post-fabrication assembly approach, in which optical waveguides and actuators are separately fabricated, faces potential challenges in optical coupling efficiency, while the mechanical stability of their connection depends critically on adhesive bonding or self-coiling adhesion properties.

3.2.2 | Monolithic Fabrication

Monolithic fabrication joins the waveguide and actuator during the same processing sequences. This technique produces structures with enhanced interfacial stability and reduced optical coupling losses. There are three main methods: embedded casting, in situ additive growth, and in situ subtractive shaping.

In embedded casting, a waveguide is placed into an uncured matrix, and curing integrates the two parts together. Tapered fibers are preferred because they keep the total thickness small. Xiao et al. and Ma et al. embedded tapered optical fibers within PDMS (Figure 4c) [36, 91], while He et al. embedded them in LCE [39]. Both approaches produced actuators with high structural stability, low optical transmission loss, and reduced thickness. The actuator developed by Xiao et al. has a thickness of approximately 70 μm [91]. The tapered optical fiber with a micron-scale tip enables seamless beam convergence, reducing coupling losses caused by dimensional mismatch. Moreover,

the fiber and the PDMS matrix maintain seamless contact without interfacial delamination even under 20% strain, and complete fracture requires a force of 6 N, demonstrating strong interfacial adhesion.

In-situ additive fabrication involves depositing functional layers directly on the waveguide. Zmyślony et al. immersed a fiber tip in a liquid crystal monomer bath, utilizing 405-nm UV light emitted from the fiber to polymerize and grow LCE structures (Figure 4e) [122]. Subsequent irradiation with 532-nm visible light controlled the deformation of the LCE actuator, ingeniously enabling the fiber to serve dual functions of fabricating and actuating the device. He et al. selectively etched roughened surfaces on PDMS fiber waveguides, enhanced their hydrophilicity via plasma treatment, then injected PNIPAM precursor solution into the etched segments using Teflon tubing molds and cured the assembly [92]. This achieved robust interfacial bonding between PNIAPM and PDMS, with a peel strength of 23.3 N/m, tolerance to large-angle deformation, and low optical losses in the actuator. However, the coupling between the PDMS fiber and the external commercial optical fiber suffered from high losses of 9.8 dB due to an imperfect interface and significant numerical aperture mismatch.

In situ subtractive shaping involves removing part of the waveguide so that the remaining section can move. Otani et al. directly cleaved the optical fiber tip at an oblique angle, producing an asymmetrical device that bends on heating [131]. Pevec et al. fused a phosphorus-doped fiber (SFF) with a coreless fiber (CLF), then selectively etched the assembly in 40% HF acid—leveraging the 30-times faster etching rate of phosphorus-doped regions versus pure silica—to form a leaflet-shaped silica actuator structure (Figure 4f). However, the optical coupling from 105/125 MMF to the coreless section and then to the silica leaves is not very efficient [123]. Wang et al. thermally grew a silica layer on a silicon substrate, patterned cantilever structures via UV lithography and wet etching, and released them stress-free by selective sacrificial layer etching. Subsequent processing produced an integrated optical waveguide-based actuator [82].

In summary, for monolithic fabrication, embedded casting typically ensures robust mechanical integration and efficient optical coupling, though with constrained structural design flexibility for actuators. In comparison, in situ additive and subtractive techniques offer diverse approaches tailored to the properties of waveguide or actuator materials, each exhibiting distinct advantages.

3.3 | Deformation Mechanisms

After the fabrication and integration of optical waveguides and actuators, the assembled system is ready for operation. The most common mechanism is volumetric expansion or contraction, but a uniform length change produced only limited displacement. Greater versatility is achieved in two ways: by driving several actuators independently or by turning uniform strain into bending through stress mismatch.

A practical approach to achieve complex deformation involves the coordinated deployment of multiple actuators. Zhou et al. and Zmyślony et al. achieved precise micro-motion control by independently modulating light through three optical fibers to trigger the photothermal effect or photoisomerization in LCE fibers, inducing axial contraction [37, 122]. The contraction of individual LCEs actuated by the three optical fibers can be precisely controlled, enabling multidirectional displacement and complex path tracking within the workspace with micron-scale accuracy (Figure 5a). Liu et al. developed a custom light-responsive deformable LCE optical fiber (LCEOF) [94]. Multiple LCEOFs were integrated into a twisted configuration. When all fibers contract simultaneously, the geometric constraints of the twisted structure cause the bundle to untwist in reverse, producing torsional motion in the actuator arm. By adjusting the input laser power, the torsional angle was precisely controlled over a range of 0–180°. Additionally, by arranging four LCEOFs symmetrically and independently controlling the laser input power to each fiber, macroscopic omnidirectional bending was achieved.

In a single device, bending results from a bilayer structure in which one side changes length more than the other. This stress mismatch can arise from an asymmetric optical field or intrinsic material heterogeneity. When a homogeneous photoresponsive material is irradiated by an asymmetric optical field, spatially differential response amplitudes emerge across different material layers, thereby generating interfacial stress within the heterostructure. Cheng et al. bonded the photoactuator to the sidewall of the optical fiber tip, ensuring emitted light irradiates only one actuator surface. This created a light-incident responsive layer and a light-shielded inert layer, thus inducing bending deformation through asymmetric photoresponses (Figure 5b) [120]. He et al. embedded the optical fiber at an off-center height within the actuator, dividing it into upper and lower layers of differing thickness. The thicker layer exhibits enhanced photoresponse, dominating deformation directionality, while the thinner layer with weaker photoresponse acts as an inert layer, collectively producing bending [39].

Actuators made from intrinsically heterogeneous materials form a bilayer structure comprising responsive and inert layers, which readily undergoes bending deformation even under symmetric optical illumination. When selecting materials for the responsive and inert layers, options can be chosen from either cognate or heterogeneous systems. One approach employs cognate materials with different properties—such as induced anisotropy or strategic dopant incorporation—to establish functional gradients. Wani et al. and Zmyślony et al. fabricated a bilayer heterostructure using LCE layers with orthogonal molecular alignments [121, 122]. Under illumination, the parallel-aligned LCE layer contracts along the actuator length, while the perpendicular-aligned layer expands along the same axis, inducing bending through strain mismatch (Figure 5c). Kuenstler et al. employed uniformly aligned LCE fibers and selectively generated AuNPs on one side via photoreduction of gold salts [90]. This localized region functions as a photothermally responsive layer, while the adjacent unmodified LCE segment, though chemically identical, remains thermally inert, enabling bending through differential thermal expansion. Otani et al. utilize obliquely cleaved optical fibers as photothermal actuators, where differential thermal expansion across the thickness gradient induces bending deformation [131].

An alternative strategy for heterogeneous material actuators is to pair a photoresponsive material as the active layer with

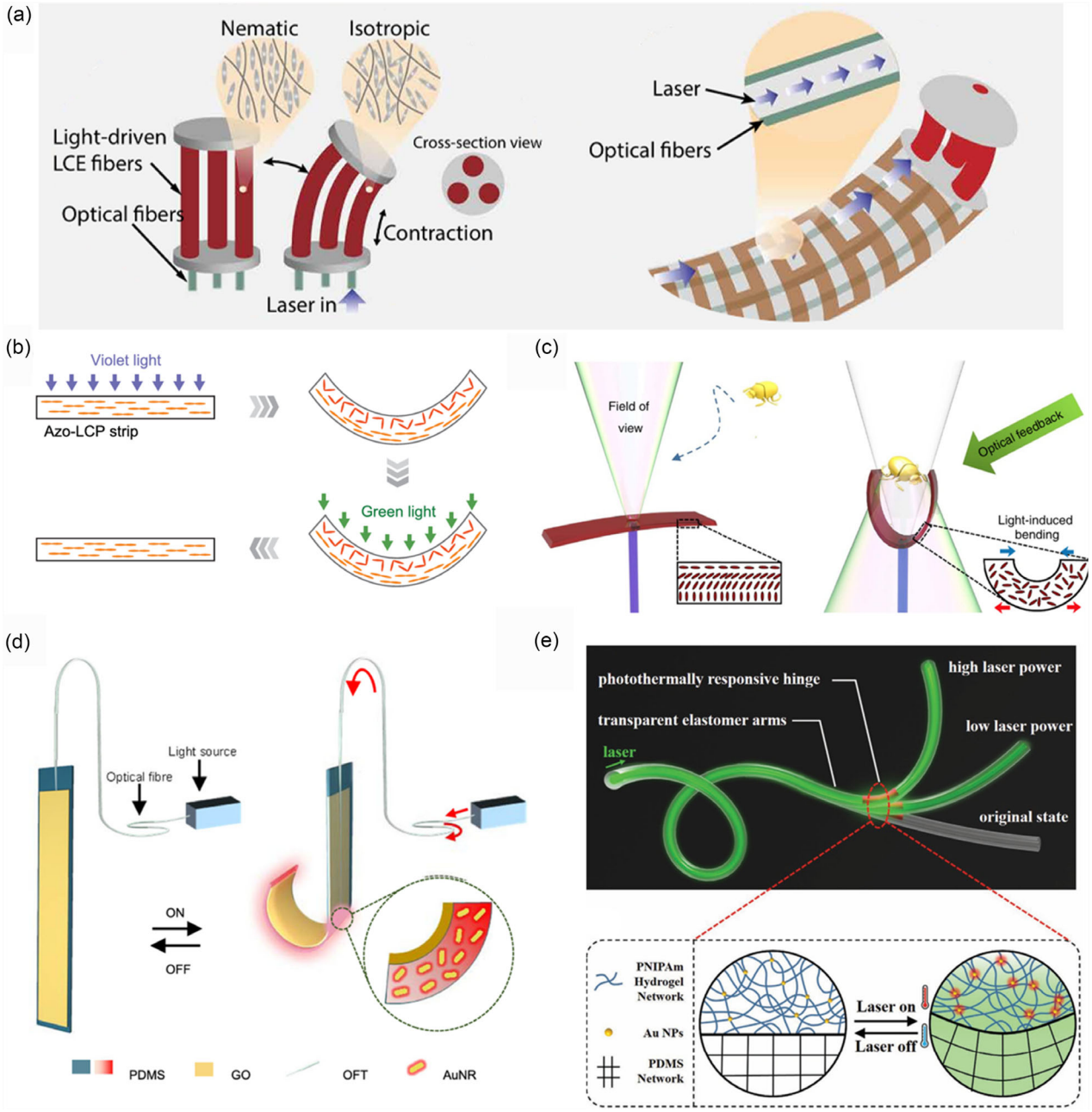

FIGURE 5 | Deformation mechanisms. (a) Three contracting LCE fibers work cooperatively to precisely control the bending angle of the actuator. Adapted with permission [37]. Copyright 2024, AAAS. (b) Asymmetric light field drives azo-LCP bending: the illuminated side undergoes photoisomerization while the opposite side remains unchanged. Reproduced with permission [120]. Copyright 2024, Wiley. (c) Orthogonally aligned bilayer LCE bends under light: One layer expands while the other contracts. Reproduced under the terms of the CC-BY license [121]. Copyright 2017, Springer Nature. (d) An actuator based on PDMS/AuNR responsive layer and GO inert layer. Reproduced under the terms of the CC-BY license [91]. Copyright 2022, Springer Nature. (e) An actuator based on PNIPAM/AuNPs responsive layer and PDMS inert layer. Reproduced with permission [92]. Copyright 2021, Wiley.

a nonresponsive material as the inert layer. This approach is used primarily with materials exhibiting isotropic photothermal expansion responses. Studies have implemented virous responsive/inert layer configurations, such as PDMS/GO (Figure 5d) [36, 91], PNIPAM/Au [38], PNIPAM/PDMS (Figure 5e) [92], PNIPAM/NOA 68 [89], SiO_2/Al [123], and SiO_2/Au [82].

Beyond volume change, other deformation mechanisms exist. For instance, devices driven by optical gradient forces can operate without volume changes, directly inducing microscopic-scale movement through photon momentum transfer [83, 132]. Furthermore, SMP rods can be twisted into helices when warmed by guided light and then retain the deformed shape upon cooling [58].

4 | Applications and Performance Analysis

4.1 | Applications

Current demonstrations of waveguide photoactuators rely on two complementary principles. First, the optical fiber acts as a flexible tether that guides the actuator through complex or confined spaces while providing mechanical traction. Second, light-induced bending provides the mechanical work needed for tasks such as grasping, lifting, and transporting objects. Together, these principles establish object transport as the core capability of the technology, and a series of specialized designs has extended this capability to include fluid pumping [38], light-feedback recognition [121], omnidirectional bending navigation [94], and crawling robots [93].

Optical fiber waveguides offer two key advantages over free-space optical control sources. First, the fixed relative position between the waveguide and actuator eliminates the need for real-time light source tracking during actuator movement. Second, waveguide-guided light transmission is immune to environmental interference in free space, enabling actuator operation along curved trajectories and within enclosed spaces. He et al. integrated the optical fiber actuator into a 1 cm-diameter silicone tube simulating the enclosed space of human blood vessels. The actuator maintained full functionality in this environment, while the flexible PDMS and PNIPAM materials prevented damage to the tube walls (Figure 6a) [92]. Zong et al. inserted the waveguide actuator into a microchannel, steered it through several bends, and demonstrated stable operation in an enclosed chamber, confirming its potential for unstructured and restricted

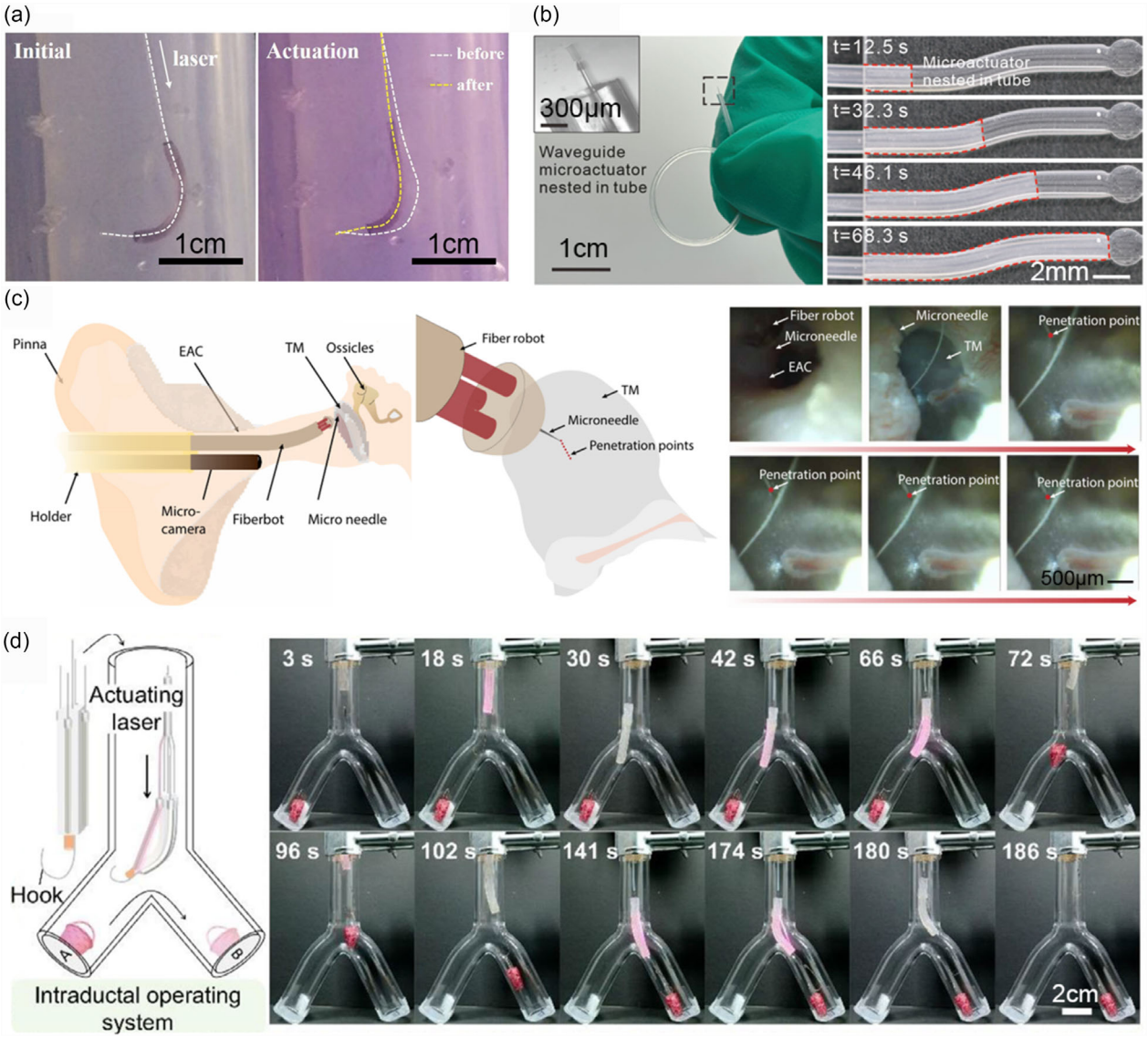

FIGURE 6 | Applications leveraging the flexibility of optical fibers. (a) Utilizing fibers to advance actuators into 1 cm diameter flexible tubes for controlled deformation. Adapted with permission [92]. Copyright 2021, Wiley. (b) Fiber-actuated systems traversing curved conduits to perform tasks. Adapted with permission [38]. Copyright 2025, Wiley. (c) In vivo otological surgery in guinea pigs using a fiber-actuator system integrated with micro-camera assembly. Adapted with permission [37]. Copyright 2024, AAAS. (d) Transfer of an object from one channel to another in a Y-shaped tube using an LCE optical fiber actuator. Adapted with permission [94]. Copyright 2025, Wiley.

settings (Figure 6b) [38]. Further, a motorized stage can translate the fiber with submicrometer precision, enabling precise micromanipulation at the microscopic scale. Otani et al. used this arrangement to assemble 100 μm diameter microspheres into programmed 2D or 3D configurations [131].

When several fibers are bundled and actuated externally, omnidirectional bending can be achieved. Zhou et al. arranged three LCE fibers at 120° intervals in a ring configuration, with both ends anchored to upper and lower platforms [37]. Each LCE fiber contains a hollow channel housing a multimode optical fiber. These fibers serve a dual function: transmitting 488 nm blue light to trigger LCE photoisomerization for microscale precision control and being pushed/pulled by external motors to induce macroscale structural bending—with no interference between micro- and macroscale actuation modes. This system, integrated with a microcamera assembly within a catheter, was tested in vivo in guinea pig ear canals, demonstrating feasibility for minimally invasive otological surgery (Figure 6c). Liu et al. utilized the LCEOF bundle with omnidirectional bending capability, integrating an endoscopic camera for navigation and a laser writing head to perform laser drilling and form letters inside a confined tube [94]. Additionally, they attached a curved metal hook to the distal end of the LCEOF bundle. The hook can safely contact and securely grasp objects and then transfer them from one branch to another within a Y-shaped tube. Both steering and grasping motions are independently controlled by the LCEOF bundle (Figure 6d). The actuator's capability to integrate a camera and navigate through Y-shaped tubes enables it to overcome navigation challenges in confined spaces, as the operator can identify and select branching paths.

Most optical waveguide-based actuators primarily rely on bending deformation, with their object-manipulation capabilities determined by bending performance. For actuators with limited bending angles (typically <40°), two or more actuator blades are combined into a clamp-like configuration, enabling object grasping with minimal deformation amplitudes. Using a microgripper composed of two azo-LCP strips, Cheng et al. successfully grasped and manipulated a 15 mm-long, 125 μm-diameter optical fiber (weight ≈0.4 mg) [120]. The full operational sequence—grasping, lifting, transferring, and releasing—was achieved, with the manipulated fiber weighing over 60 times the gripper's self-weight, demonstrating its capability to handle heavy micro-objects (Figure 7a). Zmyślony et al. fabricated opposing gripper jaws by growing bent LCE actuators on two optical fiber tips, bonded with UV-curable adhesive [122]. With jaw dimensions ≈75 μm (comparable to ant mandibles), this micro-tweezer is suitable for manipulating microelectronic components or biological cells, with a gripping force on the order of 10^{-7} N. Pevec et al. fabricated silica blades via etching and coated them with a photothermally active aluminum layer to achieve gripping motions [123]. This system successfully grasped and transferred a 125 μm-diameter, 3 mm-long optical fiber segment, demonstrating both longitudinal and transverse manipulation modes with a maximum gripping force at ≈190 μN (Figure 7b). The underwater micro-gripper developed by *Zhen* et al. consists of an optical waveguide actuator and a rigid arm [99]. The gripping force increases linearly with light power, reaching a maximum of ≈40 μN, enabling the grasping of zebrafish embryos weighing around 0.5 mg. *Li* et al. fabricated bending units using contractile LCE optical fibers and polypropylene (PP) sheets [93]. Four such bending units were symmetrically integrated onto a polymethyl methacrylate (PMMA) circular base disk. Depending on the orientation of the bending units, two types of manipulators were constructed: a forward-gripper and a reverse-hooking device. The forward-gripper bends inward to envelop and grasp objects, while the reverse-hooking bends outward, making it suitable for retrieving ring-shaped objects.

When an actuator achieves a sufficiently large bending angle, it can manipulate objects individually without requiring a partner. With increasing bending angle, the operational capability progresses sequentially from hooking to clamping and finally to coiling, accompanied by a corresponding increase in grip stability. Zhou et al. fabricated a microhook actuator (≈1 mm in length) using patterned PNIPAM/AuNPs composite hydrogel as the responsive layer and optical adhesive NOA 68 as the inert layer [89]. During free-standing operation, laser illumination triggered PNIPAM contraction, extending the hook to 145°, while laser deactivation induced PNIPAM rehydration, retracting the hook to ≈ 90°. This micro-hook successfully engaged and lifted a micro-ring, generating an output torque of 2×10^{-12} N·m. Similarly, He et al. developed a fiber-shaped actuator using PNIPAM/AuNPs as the responsive layer and PDMS as the inert layer [92]. Under laser illumination, the fiber extended to ≈180°, while deactivating the laser triggered hooking of a ring-shaped target (inner diameter, 1 cm; mass, 25 mg) with maintained ≈90° bending. In another study, He et al. implemented a photothermal LCE film actuator hook with off-center embedded optical fibers, where bending direction aligns with the fiber orientation [39]. The hook remains straight without laser illumination but undergoes bending exceeding 90° under laser activation due to asymmetric LCE contraction, lifting a 181.8 mg basket equivalent to 30 times of its own weight (Figure 7c).

Grasping with a single actuator requires bending deformation approaching 180°, demanding greater deformability than hook-type actuators. Wani et al. developed a gripper actuator by fabricating LCE films with orthogonally oriented surfaces [121]. Under illumination, depth-dependent photoisomerization of azobenzene induces asymmetric deformation, while an optical fiber fixed perpendicularly at the film center delivers light energy. This design enables the gripper's opening angle to reduce from ≈120° to 0° under optimized conditions, realizing object grasping functionality (Figure 7d). Coiling functionality demands even greater bending capability, typically above 270°. Xiao et al. fabricated an actuator with large deformation using PDMS/AuNRs as the responsive layer and GO as the inert layer, with an embedded tapered optical fiber [91]. Upon laser activation, the microactuator coiled around an ant with ≈270° bending, subsequently removing it from a needle tip (Figure 7e). Due to low optical propagation losses in the PDMS layer, the entire actuator length (≈10 mm) undergoes light-induced bending, though deformation amplitude diminishes with increasing distance due to optical attenuation. By grading the AuNR concentration along the length, Ma et al. compensated optical attenuation and obtained uniform heating over 50 mm, reaching a bending angle of about 450° and carrying 32 mg, 36 times the self-weight (Figure 7f) [36].

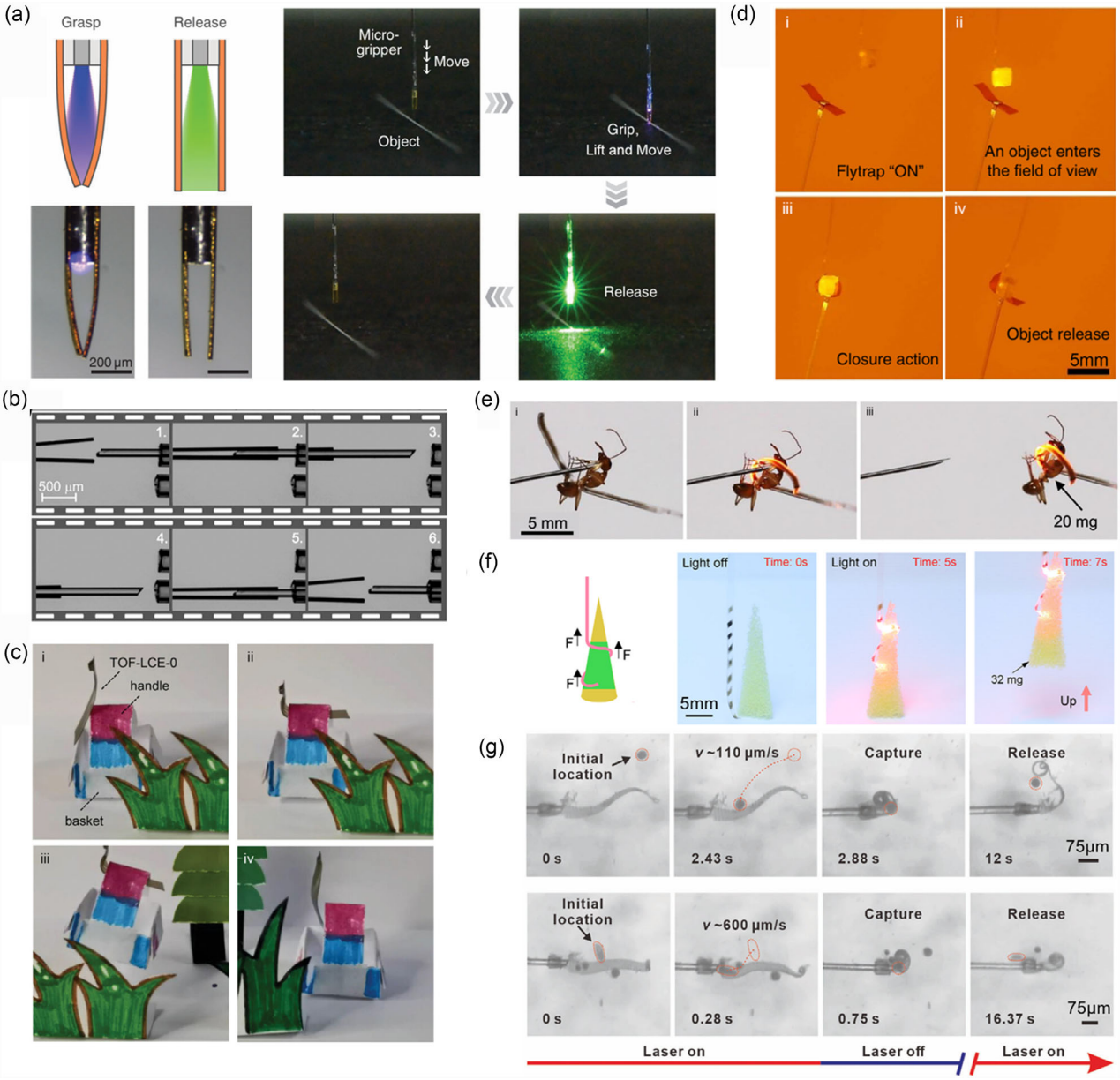

FIGURE 7 | Object manipulation applications. (a) A microgripper composed of two azo-LCP strips. Adapted with permission [120]. Copyright 2024, Wiley. (b) A gripper composed of two silica blades. Adapted with permission [123]. Copyright 2019, Optical Society of America. (c) A hook composed of a photothermal LCE film. Adapted with permission [39]. Copyright 2024, Wiley. (d) A LCE gripper actuated by reflected light from the target. Adapted under the terms of the CC-BY license [121]. Copyright 2017, Springer Nature. (e) A waveguide photoactuator based on PDMS/AuNRs and GO which can grasp an ant. Adapted under the terms of the CC-BY license [91]. Copyright 2022, Springer Nature. (f) A waveguide photoactuator based on PDMS/AuNRs and GO which can grasp a conical object utilizing large bending angle Adapted with permission [36]. Copyright 2025, Wiley. (g) A waveguide photoactuator based on PNIPAM and Au which can capture dynamic targets. Adapted with permission [38]. Copyright 2025, Wiley.

Beyond static object manipulation, waveguide photoactuators can effectively capture dynamic targets when designed for sufficient response speed. Zong et al. employed an ultra-thin PNIPAM hydrogel responsive layer (≈3 μm) and a 5 nm-thick gold film as the inert layer, achieving both high deformation angles (max 800°) and ultrafast actuation (0.55 s grasping cycle) [38]. This micro-actuator successfully captured swimming spherical Chlamydomonas (110 μm/s) and sole-shaped paramecium (600 μm/s) (Figure 7g).

Certain waveguide photoactuators exhibit programmable deformation modes. One programmable control strategy leverages the alignment process of anisotropic LCEs. He et al. embedded tapered optical fibers within LCE matrices and then mechanically stretched the LCE along distinct axes to fabricate actuators with 0°, 45°, and 90° orientation angles relative to the fiber direction [39]. By integrating these directionally programmed bending actuators, they constructed a bionically inspired hand architecture capable of executing intricate gestures through coordinated multilaser control (Figure 8a). An alternative control strategy utilizes patterned rigid inert layers to guide deformation direction. Ma et al. modified PDMS surfaces with PI masks restricting modification zones, enabling selective GO adhesion only on treated regions [36]. By varying GO patterns,

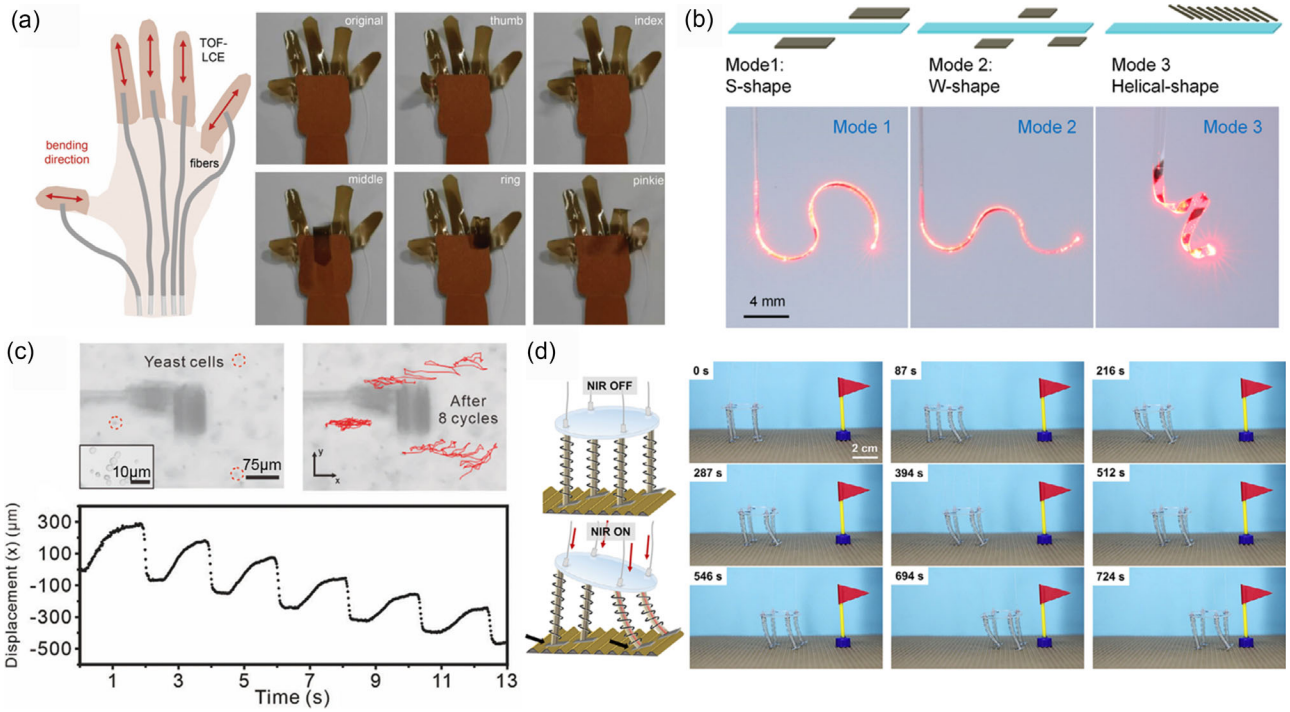

FIGURE 8 | Programmable deformation and other applications. (a) A bionic hand demonstration composed of LCEs stretched along different axes. Adapted with permission [39]. Copyright 2024, Wiley. (b) Multimode deformations of the actuators with different GO patterns. Adapted with permission [36]. Copyright 2025, Wiley. (c) Performance of eight pumping cycles on yeast cells in the microenvironment by the waveguide actuator, and displacement measurement of the yeast cells along the *x*-axis during the pumping cycles. Adapted with permission [38]. Copyright 2025, Wiley. (d) The crawling device based on LCE optical fiber actuators. Adapted with permission [93]. Copyright 2025, Wiley.

they fabricated actuators exhibiting S-shaped, W-shaped, and helical deformations (Figure 8b). Zong et al. employed UV lithography to pattern PNIPAM hydrogel-based actuators, with additional SU-8 rigid strip structures photolithographically patterned on their surfaces [38]. The fundamental configuration features SU-8 strips perpendicular to the actuator length, while alternatively, tilted SU-8 strips combined with programmable hydrogel patterning induce helical deformations. In addition, replacing strips with rigid SU-8 panels enabled the applications of compressive mechanical stimulation to cells.

Certain waveguide photoactuators achieve advanced functionality through structural innovations. Wani et al. introduced a transparent window at the fiber–LCE interface [121]. Light emitted from the optical fiber is reflected or scattered by external objects, and the reflected light is absorbed by the actuator, inducing deformation. This mechanism enables light-feedback recognition (Figure 7d). In microscale fluidic environments where the Reynolds number is low and viscous forces dominate over inertial forces, reciprocal motion cannot generate net displacement due to the Scallop Theorem. When activated, Zong et al.'s waveguide actuator heats up by emitting 1550 nm infrared laser light from a tapered optical fiber to locally warm the surrounding aqueous microenvironment; when deactivated, it cools through uniform heat dissipation into the ambient environment [38]. Due to the asymmetry between heating and cooling mechanisms, the motion trajectory of the actuator does not coincide over one laser on–off cycle, resulting in an enclosed non-reciprocal area. This enables the transport of yeast cells in microfluidic environment (Figure 8c). Waveguide actuators have also achieved terrestrial crawling functionality. Li et al. utilized four LCE optical fiber bending units, achieving forward locomotion by alternately activating different actuator elements to generate asymmetric friction forces and alternating changes in support points [93]. This crawling mechanism relies on mechanical interlocking with grooves on the ground surface (Figure 8d). Although the system exhibited relatively slow movement—traversing 8 cm in 724 s—it successfully demonstrates the potential application of waveguide actuators in the field of autonomous mobile robotics. Additionally, actuators based on integrated optical waveguides hold application potential within photonic integrated circuits [45, 82, 117, 118, 132].

4.2 | Performance Analysis

The performance of waveguide photoactuators is evaluated based on key metrics including size, maximum deformation angle, response time, driving power, output force, repeatability, and operational medium. Representative values of these parameters for reported devices are summarized in Table 1.

Figure 9 catalogs existing waveguide photoactuators by photoresponsive material type, maximum bending angle and actuation time. The color coding represents material systems: blue for thermal expansion mechanisms, green for PNIPAM hydrogels, and red for LCE actuators. Overall, significant performance distinctions exist among different photoresponse mechanisms. The deformation rate of waveguide photoactuators is defined as the bending angle change per unit time. Actuators positioned

TABLE 1 | Size, maximum deformation angle, response time, driving power, output force, and cycling stability of current waveguide photoactuators.

Photoresponsive materials	Average thickness (μm)	Average length (mm)	Maximum deformation angle (°)	Actuation time for maximum deformation (s)	Recovery time for maximum deformation (s)	Actuation power (mw)	Output force (μN)	Cycling stability	Reference
SMP	400	15	Mold-dependent	3	NA	4890 in water/600 in air	NA	NA	[58]
Plastic	500	10	≈0.4	≈0.15	≈0.15	35	100 (grasping)	Stable for dozens of cycles	[131]
SiO2	0.6	0.2	≈0.1	≈0.005	≈0.005	0.25	NA	Stable for 100–400 Hz short-term cycling	[82]
PNIPAM	35	1	60	60	120	278	0.006 (loading)	Stable for hundreds of cycles	[89]
LCE	20	5	120	0.2	1	300	300 (grasping)	Stable for several cycles	[121]
LCE	750	20	14	3.3	7.7	230	NA	Stable for several cycles	[90]
Al	30	3.5	≈2.2	0.8	0.8	135	190 (grasping)	NA	[123]
LCE	50	0.27	20	0.1	1	9	>0.1 (grasping)	Stable for 400 cycles	[122]
PNIPAM	275	7	145	180	480	800	10 (loading)	Deformation angle decayed to 85% after 1st cycle	[92]
PDMS	70	10	270	2.4	≈8	150	400 (single arm bending)	Stable for 3000 cycles	[91]
LCE	30	10	150	10	10	80	1800 (loading)	Deformation angle decayed to 47% after 100 cycles	[39]
LCE	300	1.6	≈5.4	6	4	15	35 000 (single fiber loading)	Stable for 300 cycles	[37]
LCE	20	0.5	≈38	30	30	2.4 for UV /5.9 for Vis	4 (loading)	Stable for several cycles	[119]
PNIPAM	4	0.3	800	0.55	2	8	NA	Stable for 1000 cycles	[38]

(Continues)

TABLE 1 | (Continued)

Photoresponsive materials	Average thickness (μm)	Average length (mm)	Maximum deformation angle (°)	Actuation time for maximum deformation (s)	Recovery time for maximum deformation (s)	Actuation power (mw)	Output force (μN)	Cycling stability	Reference
PDMS	75	50	450	2.3	3	170	300 (loading)	NA	[36]
LCE	600	30	64	20	20	767	12 000 (single fiber loading)	Deformation length decayed to 88% after 200 cycles	[93]
LCE	770	50	55	12	48	790	60 000 (single fiber loading)	Deformation length decayed to 82% after 70 cycles	[94]
PDMS	150	5	158 in air/66 in water	1.8	7	160	40 (grasping)	Stable for 1000 cycles	[99]

FIGURE 9 | Actuation time versus maximum deformation angle of current waveguide photoactuators. The color of the dots represents the used photoresponsive materials.

closer to the bottom-right quadrant of the figure exhibit higher deformation rates. Zong et al. achieved the fastest rate exceeding 1400°/s [38], while other high-speed actuators operated within the 100°–600°/s range. The PNIPAM-based actuators achieved exceptional deformation rates—far surpassing other systems—by leveraging both high swelling ratios for large bending angles and ultrathin architectures enabling ultrafast thermal/water diffusion kinetics. The LCE-based actuators by Zmyślony et al. and Wani et al. attained high angular speeds due to sub-micron thickness and rapid photoresponsive materials, minimizing activation time [121, 122]. The PDMS-based actuators by Xiao et al. and Ma et al. also acted as optical waveguides, permitting extended lengths (>50 mm) where light propagates to distal segments, thereby amplifying total deformation angles and rates [36, 91]. For waveguide photoactuators with slower deformation rates, the primary limiting factors include thermal conduction and mass transport timescales. Thicker structures exhibit constrained heating rates, while cooling typically lags behind heating—prolonging switching cycles. In millimeter-scale PNIPAM hydrogels, slow water absorption/desorption kinetics significantly extends response times. Additionally, material viscoelasticity and relaxation effects delay shape recovery.

The output force of the waveguide actuators is presented in Table 1. Due to differences in actuator structure and experimental methodology, the reported values are described using different metrics, with specific meanings indicated in parentheses. For example, “grasping force” refers to the clamping force applied by the actuator, while “loading force” represents the weight of an object lifted by the actuator. Among them, the LCE fiber-based actuator demonstrates the highest output force [37, 93, 94]. All three studies utilized the contractile deformation of LCE for output force testing, which may lead to better results compared to actuators relying on bending-based mechanisms. A comprehensive evaluation of actuator efficiency should incorporate multiple factors, including output force, input energy, actuator dimensions and magnitude of deformation.

In repeated cycling tests, waveguide photoactuators have demonstrated stable performance retention over hundreds to thousands of cycles in numerous studies. However, durability assessments remain absent in several current investigations. Wani et al. revealed that under high-power illumination or prolonged operation, photothermal heating softens LCEs, causing temporary adhesion that prevents full recovery to the initial state after light deactivation—thereby reducing deformation efficiency in subsequent cycles. A 45°C annealing process was required for recovery [121]. In the study by He et al., the actuator exhibited an initial deformation angle decay to 85% after the first cycle, resulting from irreversible hydrogen bond disruption and hydrophobic interaction fractures within the PNIPAM hydrogel during repeated phase transitions, compounded by limited mass transport and thermal conduction in its thick structure [92]. In another study by He et al., the deformation angle attenuated to 41%–47% after 100 cycles, attributed to photochemical degradation and agglomeration of bismuth-doped LCE under high-temperature cycling, which reduced photothermal conversion efficiency [39].

The operating medium dictates the applicable environments for waveguide photoactuators. Hydrogel actuators necessarily operate in aqueous environments due to their reliance on water absorption/desorption for deformation. Beyond this, most other waveguide actuators are tested and deployed in air. To broaden device applicability, nonhydrogel actuators have also been investigated for their operational performance in liquid environments. For example, Otani et al. demonstrated that angled-cleaved fiber actuators show no significant performance degradation in aquatic environments. Instead, accelerated heat dissipation enabled faster shape recovery after grasping operations [131]. Zhou et al. successfully performed surgical experiments in live biological environments without operational interference from liquid media [37]. However, for most non-hydrogel waveguide photoactuators, transitioning from air to aquatic environments requires higher laser power to achieve equivalent deformation, as water's high specific heat capacity accelerates heat dissipation. For instance, in the study by Small et al., SMP actuator required only 0.60 W in air but 4.89 W in water, with an extended activation time [58]. A potential solution is inspired by animals such as otters, which trap a layer of air using their superhydrophobic fur for thermal insulation underwater [133]. Zhen et al. coated the actuator surface with an approximately 50 μm thick layer of hydrophobic silica aerogel as a thermal barrier [99]. When immersed in water, a stable air layer around 100 μm thick forms on the surface, which significantly reduces heat dissipation from the actuator into the water. This promotes heat accumulation within the actuator, leading to a substantial temperature increase and ultimately enabling successful deformation. Concurrently, water's elevated refractive index reduces the critical angle for total internal reflection, increasing optical loss; additionally, hydrodynamic drag and material stability in aqueous media also significantly influence overall performance.

5 | Conclusion and Outlook

This review has examined the current status of waveguide photoactuators, defined as devices that guide light through a waveguide to a photoresponsive material, converting optical energy into mechanical deformation. By replacing free-space illumination with fiber or planar waveguides, these actuators overcome two persistent obstacles: optical loss in scattering media and the need for active beam tracking. The low-loss, confined light delivery allows precise spatial control and reliable operation in narrow or tortuous settings. We have summarized the classes of photoresponsive materials used in practical applications, including photothermal polymers such as LCEs, SMPs, and hydrogels; photochemical systems based on azobenzene; and, on the microscale, structures driven directly by optical forces. Corresponding waveguides include commercial silica fibers, POFs, tapered MNFs, and integrated optical waveguides. Integration strategies fall into two broad groups: monolithic methods, which embed or grow the actuator on the waveguide, and post-assembly methods, which attach the two parts by adhesives or self-coiling films. Most reported devices generate bending through stress mismatch, created either by an asymmetric optical field or bilayer heterostructures, with demonstrated applications focusing on grasping, transporting, and releasing small objects.

Despite these advances, the field remains in its early stage of development. Many photoresponsive materials have not yet been integrated with waveguides; to date, only photothermal LCEs, azobenzene-modified LCEs, PNIPAM hydrogels, and PDMS composites have been explored in depth. Most published prototypes rely on optical fiber waveguides, whereas planar waveguide actuators fabricated by standard photonic processes have attracted little attention. Key integration challenges, including optical coupling efficiency, scattered-light loss, and the mechanical strength of the fiber-actuator interface, require systematic investigation, especially for use in confined environments. Functionally, unidirectional bending remains dominant actuation mode, with more complex behaviors such as multi-axis coordination or patterned anisotropy appearing only in isolated studies.

Performance varies widely across different systems. Thinner structures deliver larger bending angles and faster response times, supporting true microscale manipulation; however, long-term durability under repeated thermal cycling often remains unverified. For applications in liquid media, which is a regime where waveguides offer clear advantages over free-space optics, data on nonhydrogel systems are still scarce. In addition, the optical tether that delivers light also restricts mobility: Waveguide photoactuators typically require external pulling or positioning rather than operating as freely moving devices. Several research groups have begun to integrate cameras for visual feedback; future work could utilize the same fiber for back-reflected light sensing or combine optical power delivery with electrical or acoustic signals to create multifunctional tools.

Continued progress will therefore depend on three priorities: broadening the range of waveguide-compatible materials, improving optical and mechanical integration to raise efficiency and robustness, and diversifying deformation modes to extend functionality beyond simple gripping. Addressing these challenges is expected to advance waveguide photoactuators from laboratory prototypes toward practical devices for applications such as minimally invasive medicine, cell manipulation, and high-precision micro-assembly.

Acknowledgments

This work is supported by the National Key Technologies R&D Program of China (2022YFA1207000, 2022YFA1404700, and 2021YFA0715302), the National Natural Science Foundation of China (52101214 and 62375054), the Shanghai Rising-Star Program (24QA2700700), the Science and Technology Commission of Shanghai Municipality (24520750200 and 24CL2900200), and the Shanghai Talent Programs.

Conflicts of Interest

The authors declare no conflicts of interest.

References

1. M. R. A. Bhatti, A. Kernin, M. Tausif, et al., "Light-Driven Actuation in Synthetic Polymers: A Review from Fundamental Concepts to Applications," *Advanced Optical Materials* 10, no. 10 (2022): 2102186, https://doi.org/10.1002/adom.202102186.

2. T. Zhan, H. Xie, J. Mao, et al., "Conductive PNIPAM/CMCS/MWCNT/PANI Hydrogel with Temperature, Pressure and pH Sensitivity," *ChemistrySelect* 6, no. 17 (2021): 4229–4237, https://doi.org/10.1002/slct.202101003.

3. Y. Shi, C. Ma, L. Peng, et al., "Conductive "Smart" Hybrid Hydrogels with PNIPAM and Nanostructured Conductive Polymers," *Advanced Functional Materials* 25, no. 8 (2015): 1219–1225, https://doi.org/10.1002/adfm.201404247.

4. M. Li, X. Wang, B. Dong, et al., "In-Air Fast Response and High Speed Jumping and Rolling of a Light-Driven Hydrogel Actuator," *Nature Communications* 11, no. 1 (2020): 3988, https://doi.org/10.1038/s41467-020-17775-4.

5. H. Na, Y. W. Kang, C. S. Park, et al., "Hydrogel-Based Strong and Fast Actuators by Electroosmotic Turgor Pressure," *Science* 376, no. 6590 (2022): 301–307, https://doi.org/10.1126/science.abm7862.

6. M. M. Hamedi, V. E. Campbell, P. Rothemund, et al., *Electrically Activated Paper Actuators. Advanced Functional Materials* 26, no. 15 (2016): 2446–2453, https://doi.org/10.1002/adfm.201505123

7. A. H. Gelebart, D. Jan Mulder, M. Varga, et al., "Making Waves in a Photoactive Polymer Film," *Nature* 546, no. 7660 (2017): 632–636, https://doi.org/10.1038/nature22987.

8. L. Lan, L. Li, Q. Di, et al., "Organic Single-Crystal Actuators and Waveguides that Operate at Low Temperatures," *Advanced Materials* 34, no. 14 (2022): 2200471, https://doi.org/10.1002/adma.202200471.

9. Z. J. Wang, C. Y. Li, X. Y. Zhao, et al., "Thermo- and Photo-Responsive Composite Hydrogels with Programmed Deformations," *Journal of Materials Chemistry B* 7, no. 10 (2019): 1674–1678, https://doi.org/10.1039/C8TB02896F.

10. C. Y. Li, D. Jiao, X. P. Hao, et al., "Bistable Joints Enable the Morphing of Hydrogel Sheets with Multistable Configurations," *Advanced Materials* 35, no. 15 (2023): 2211802, https://doi.org/10.1002/adma.202211802.

11. Z. Wang, Z. Wang, Y. Zheng, et al., "Three-Dimensional Printing of Functionally Graded Liquid Crystal Elastomer," *Science Advances* 6, no. 39 (2020): eabc0034, https://doi.org/10.1126/sciadv.abc0034.

12. N. Hu, B. Li, R. Bai, et al., "A Torsion-Bending Antagonistic Bistable Actuator Enables Untethered Crawling and Swimming of Miniature Robots," *Research; a Journal of Science and Its Applications* 6 (2023): 0116, https://doi.org/10.34133/research.0116.

13. Q. Liu, W. Wang, M. F. Reynolds, et al., "Micrometer-Sized Electrically Programmable Shape-Memory Actuators for Low-Power Microrobotics," *Science Robotics* 6, no. 52 (2021): eabe6663, https://doi.org/10.1126/scirobotics.abe6663.

14. Q. Liu, W. Wang, H. Sinhmar, et al., "Electronically Configurable Microscopic Metasheet Robots," *Nature Materials* 24, no. 1 (2025): 109–115, https://doi.org/10.1038/s41563-024-02007-7.

15. N. Ebrahimi, C. Bi, D. J. Cappelleri, et al., "*Magnetic Actuation Methods in Bio/Soft Robotics*," *Advanced Functional Materials* 31, no. 11 (2021): 2005137, https://doi.org/10.1002/adfm.202005137.

16. J. Cui, T.-Y. Huang, Z. Luo, et al., "Nanomagnetic Encoding of Shape-Morphing Micromachines," *Nature* 575, no. 7781 (2019): 164–168, https://doi.org/10.1038/s41586-019-1713-2.

17. Y.-W. Lee, J.-K. Kim, U. Bozuyuk, et al., "Multifunctional 3D-Printed Pollen Grain-Inspired Hydrogel Microrobots for On-Demand Anchoring and Cargo Delivery," *Advanced Materials* 35, no. 10 (2023): 2209812, https://doi.org/10.1002/adma.202209812.

18. Z.-C. Ma, Y.-L. Zhang, B. Han, et al., "Femtosecond Laser Programmed Artificial Musculoskeletal Systems," *Nature Communications* 11, no. 1 (2020): 4536, https://doi.org/10.1038/s41467-020-18117-0.

19. X. Yang, L. Lan, X. Pan, et al., "Bioinspired Soft Robots Based on Organic Polymer-Crystal Hybrid Materials with Response to Temperature and Humidity," *Nature Communications* 14, no. 1 (2023): 2287, https://doi.org/10.1038/s41467-023-37964-1.

20. T. Xu, D. Pei, S. Yu, et al., "Design of MXene Composites with Biomimetic Rapid and Self-Oscillating Actuation under Ambient Circumstances," *ACS Applied Materials & Interfaces* 13 (2021): 31978–31985, https://doi.org/10.1021/acsami.1c06343.

21. D.-D. Han, Y.-L. Zhang, J.-N. Ma, et al., "Light-Mediated Manufacture and Manipulation of Actuators," *Advanced Materials* 28, no. 38 (2016): 8328–8343, https://doi.org/10.1002/adma.201602211.

22. J. Li, X. Zhou, and Z. Liu, "Recent Advances in Photoactuators and Their Applications in Intelligent Bionic Movements," *Advanced Optical Materials* 8, no. 18 (2020): 2000886, https://doi.org/10.1002/adom.202000886.

23. G. Stoychev, A. Kirillova, and L. Ionov, "Light-Responsive Shape-Changing Polymers," *Advanced Optical Materials* 7, no. 16 (2019): 1900067, https://doi.org/10.1002/adom.201900067.

24. B. Han, Y.-L. Zhang, Q.-D. Chen, et al., *Carbon-Based Photothermal Actuators. Advanced Functional Materials* 28, no. 40 (2018): 1802235, https://doi.org/10.1002/adfm.201802235.

25. Y. Hu, G. Wu, T. Lan, et al., "A Graphene-Based Bimorph Structure for Design of High Performance Photoactuators," *Advanced Materials* 27, no. 47 (2015): 7867–7873, https://doi.org/10.1002/adma.201502777.

26. J. Mu, C. Hou, H. Wang, et al., "Origami-Inspired Active Graphene-Based Paper for Programmable Instant Self-Folding Walking Devices," *Science Advances* 1, no. 10 (2015): e1500533, https://doi.org/10.1126/sciadv.1500533.

27. T. Wang, D. Torres, F. E. Fernández, et al., "Increasing Efficiency, Speed, and Responsivity of Vanadium Dioxide Based Photothermally Driven Actuators Using Single-Wall Carbon Nanotube Thin-Films," *ACS Nano* 9, no. 4 (2015): 4371–4378, https://doi.org/10.1021/acsnano.5b00873.

28. Y. Takashima, S. Hatanaka, M. Otsubo, et al., "Expansion–contraction of Photoresponsive Artificial Muscle Regulated by Host–guest Interactions," *Nature Communications* 3, no. 1 (2012): 1270, https://doi.org/10.1038/ncomms2280.

29. R. Medishetty, A. Husain, Z. Bai, et al., "Single Crystals Popping under UV Light: A Photosalient Effect Triggered by a [2+2] Cycloaddition Reaction," *Angewandte Chemie (international Ed. in English)* 53, no. 23 (2014): 5907–5911, https://doi.org/10.1002/anie.201402040.

30. L. Tang, L. Wang, X. Yang, et al., "*Poly(N-Isopropylacrylamide)-Based Smart Hydrogels: Design, Properties and Applications.*," *Progress in Materials Science* 115 (2021): 100702, https://doi.org/10.1016/j.pmatsci.2020.100702.

31. L. Qin, X. Liu, and Y. Yu, "*Soft Actuators of Liquid Crystal Polymers Fueled by Light from Ultraviolet to Near Infrared*," *Advanced Optical Materials* 9, no. 7 (2021): 2001743, https://doi.org/10.1002/adom.202001743.

32. L. Luo, F. Zhang, L. Wang, et al., "Recent Advances in Shape Memory Polymers: Multifunctional Materials, Multiscale Structures, and Applications," *Advanced Functional Materials* 34, no. 14 (2024): 2312036, https://doi.org/10.1002/adfm.202312036.

33. L. Zhang, Y. Zhen, and L. Tong, "Optical Micro/Nanofiber Enabled Tactile Sensors and Soft Actuators: A Review," *Opto-Electronic Science* 3, no. 8 (2024): 240005–240005, https://doi.org/10.29026/oes.2024.240005.

34. Y. Hu, Q. Ji, M. Huang, et al., Light-Driven Self-Oscillating Actuators with Phototactic Locomotion Based on Black Phosphorus Heterostructure," *Angewandte Chemie International Edition*, 60 (2021): 20511–20517, https://doi.org/10.1002/anie.202108058.

35. Y. Zhao, C. Xuan, X. Qian, et al., "Soft Phototactic Swimmer Based on Self-Sustained Hydrogel Oscillator," *Science Robotics* 4, no. 33 (2019): eaax7112, https://doi.org/10.1126/scirobotics.aax7112.

36. S. Ma, J. Xiao, X. Song, et al., "Multimode and Programmable Deformation of Optical Fiber Taper-Based Waveguide Photoactuators," *Advanced Optical Materials* 13 (2025): 2500718, https://doi.org/10.1002/adom.202500718.

37. C. Zhou, Z. Xu, Z. Lin, et al., "Submillimeter Fiber Robots Capable of Decoupled Macro- Micro Motion for Endoluminal Manipulation," *Science Advances* 10 (2024): eadr6428, https://doi.org/10.1126/sciadv.adr6428.

38. Y. Zong, M. Xi, Y. Wang, et al., "*Waveguide Microactuators Self-Rolled Around an Optical Fiber Taper.*," *Advanced Materials* 37, no. 12 (2025): 2418316, https://doi.org/10.1002/adma.202418316.

39. Y. He, H. Liu, J. Luo, et al., "*Liquid Crystal Elastomer Actuators Enhanced by Tapered Optical Fibers for Controllable Bending Directions and Amplitudes*," *Advanced Materials Technologies* 9, no. 13 (2024): 2400073, https://doi.org/10.1002/admt.202400073.

40. S. Nocentini, C. Parmeggiani, D. Martella, et al., *Optically Driven Soft Micro Robotics. Advanced Optical Materials* 6, no. 14 (2018): 1800207, https://doi.org/10.1002/adom.201800207.

41. Y. Wang, J. Liu, and S. Yang, "Multi-Functional Liquid Crystal Elastomer Composites," *Applied Physics Reviews* 9, no. 1 (2022): 011301, https://doi.org/10.1063/5.0075471.

42. X. Pang, J. Lv, C. Zhu, et al., "Photodeformable Azobenzene-Containing Liquid Crystal Polymers and Soft Actuators," *Advanced Materials* 31, no. 52 (2019): 1904224, https://doi.org/10.1002/adma.201904224.

43. H. A. M. Abdelmohsen, N. A. Copeland, and J. G. Hardy, "Light-Responsive Biomaterials for Ocular Drug Delivery," *Drug Delivery and Translational Research* 13, no. 8 (2023): 2159–2182, https://doi.org/10.1007/s13346-022-01196-5.

44. X.-F. Lin, G.-Q. Hu, Q.-D. Chen, et al., "A Light-Driven Turbine-Like Micro-Rotor and Study on Its Light-to-Mechanical Power Conversion Efficiency," *Applied Physics Letters* 101, no. 11 (2012): 113901, https://doi.org/10.1063/1.4751464.

45. Y. Wang, K. F. Wang, and B. L. Wang, "Bending Mechanism of Optically Actuated All-Optical Mechanical Switches Composed of Bilayer Waveguides," *International Journal of Mechanical Sciences* 222 (2022): 107234, https://doi.org/10.1016/j.ijmecsci.2022.107234.

46. Z. C. Jiang, Y. Y. Xiao, and Y. Zhao, "Shining Light on Liquid Crystal Polymer Networks: Preparing, Reconfiguring, and Driving Soft Actuators," *Advanced Optical Materials* 7, no. 16 (2019): 1900262, https://doi.org/10.1002/adom.201900262.

47. X. Liu, M. Gao, J. Chen, et al., "Recent Advances in Stimuli-Responsive Shape-Morphing Hydrogels," *Advanced Functional Materials* 32, no. 39 (2022): 2203323, https://doi.org/10.1002/adfm.202203323.

48. Y. Yang and Y. Shen, "*Light-Driven Carbon-Based Soft Materials: Principle, Robotization, and Application. Advanced Optical Materials*9, no. 12 (2021): 2100035, https://doi.org/10.1002/adom.202100035.

49. J. Chen, D. Wang, J. Xi, et al., "Immuno Gold Nanocages with Tailored Optical Properties for Targeted Photothermal Destruction of Cancer Cells," *Nano Letters* 7, no. 5 (2007): 1318–1322, https://doi.org/10.1021/nl070345g.

50. C. M. Hessel, et al., "Copper Selenide Nanocrystals for Photothermal Therapy," *Nano Letters* 11, no. 6 (2011): 2560–2566, https://doi.org/10.1021/nl201400z.

51. G. Hu, T. Xu, X. Chen, et al., "Solar-Driven Broad Spectrum Fungicides Based on Monodispersed Cu7S4 Nanorods with Strong Near-Infrared Photothermal Efficiency," *RSC Advances* 6, no. 106 (2016): 103930–103937, https://doi.org/10.1039/C6RA22737F.

52. J. S. Scarpa, D. D. Mueller, and I. M. Klotz, "Slow Hydrogen-Deuterium Exchange in a Non-.alpha.-Helical Polyamide," *Journal of the American Chemical Society* 89, no. 24 (1967): 6024–6030, https://doi.org/10.1021/ja01000a006.

53. A. Halperin, M. Kröger, and F. M. Winnik, "Poly(N-Isopropylacrylamide) Phase Diagrams: Fifty Years of Research," *Angewandte Chemie International Edition* 54 (2015):15342–15367, https://doi.org/10.1002/anie.201506663.

54. C. M. Yakacki, S. Willis, C. Luders, et al., "*Deformation Limits in Shape-Memory Polymers*," *Advanced Engineering Materials* 10, no. 1 (2008): 112–119, https://doi.org/10.1002/adem.200700184.

55. B. Xu, Y. Q. Fu, M. Ahmad, et al., "Thermo-Mechanical Properties of Polystyrene-Based Shape Memory Nanocomposites," *Journal of Materials Chemistry* 20, no. 17 (2010): 3442–3448, https://doi.org/10.1039/B923238A.

56. S. Rezanejad and M. Kokabi, "Shape Memory and Mechanical Properties of Cross-Linked Polyethylene/Clay Nanocomposites," *European Polymer Journal* 43, no. 7 (2007): 2856–2865, https://doi.org/10.1016/j.eurpolymj.2007.04.031.

57. T. Xie and I. A. Rousseau, "Facile Tailoring of Thermal Transition Temperatures of Epoxy Shape Memory Polymers," *Polymer* 50, no. 8 (2009): 1852–1856, https://doi.org/10.1016/j.polymer.2009.02.035.

58. W. Small, T. S. Wilson, W. J. Benett, et al., "*Laser-Activated Shape Memory Polymer Intravascular Thrombectomy Device*," *Optics Express* 13, no. 20 (2005): 8204–8213, https://doi.org/10.1364/opex.13.008204.

59. Y. Ji, J. E. Marshall, and E. M. Terentjev, "*Nanoparticle-Liquid Crystalline Elastomer Composites. Polymers*," 4, no. 1 (2012): 316–340, https://doi.org/10.3390/polym4010316.

60. M. Camacho-Lopez, H. Finkelmann, P. Palffy-Muhoray, et al., "Fast Liquid-Crystal Elastomer Swims into the Dark," *Nature Materials* 3, no. 5 (2004): 307–310, https://doi.org/10.1038/nmat1118.

61. S. V. Ahir, A. R. Tajbakhsh, and E. M. Terentjev, "*Self-Assembled Shape-Memory Fibers of Triblock Liquid-Crystal Polymers*," *Advanced Functional Materials* 16, no. 4 (2006): 556–560, https://doi.org/10.1002/adfm.200500692.

62. T. H. Ware, J. S. Biggins, A. F. Shick, et al., "Localized Soft Elasticity in Liquid Crystal Elastomers," *Nature Communications* 7, no. 1 (2016): 10781, https://doi.org/10.1038/ncomms10781.

63. J. Deng, J. Li, P. Chen, et al., "Tunable Photothermal Actuators Based on a Pre-Programmed Aligned Nanostructure," *Journal of the American Chemical Society* 138, no. 1 (2016): 225–230, https://doi.org/10.1021/jacs.5b10131.

64. X. Zhang, Z. Yu, C. Wang, et al., "Photoactuators and Motors Based on Carbon Nanotubes with Selective Chirality Distributions," *Nature*

Communications 5, no. 1 (2014): 2983, https://doi.org/10.1038/ncomms3983.

65. L. Chen, M. Weng, P. Zhou, et al., "Multi-Responsive Actuators Based on a Graphene Oxide Composite: Intelligent Robot and Bioinspired Applications," *Nanoscale* 9, no. 28 (2017): 9825–9833, https://doi.org/10.1039/C7NR01913K.

66. Y. Tai, G. Lubineau, and Z. Yang, "Light-Activated Rapid-Response Polyvinylidene-Fluoride-Based Flexible Films," *Advanced Materials* 28, no. 23 (2016): 4665–4670, https://doi.org/10.1002/adma.201600211.

67. L. Li, J. Meng, C. Hou, et al., "Dual-Mechanism and Multimotion Soft Actuators Based on Commercial Plastic Film," *ACS Applied Materials & Interfaces* 10, no. 17 (2018): 15122–15128, https://doi.org/10.1021/acsami.8b00396.

68. F. Barroso-Bujans, S. Cerveny, A. Alegría, et al., "Sorption and Desorption Behavior of Water and Organic Solvents from Graphite Oxide," *Carbon* 48, no. 11 (2010): 3277–3286, https://doi.org/10.1016/j.carbon.2010.05.023.

69. G. S. Kumar and D. C. Neckers, "Photochemistry of Azobenzene-Containing Polymers," *Chemical Reviews* 89, no. 8 (1989): 1915–1925, https://doi.org/10.1021/cr00098a012.

70. Z. Mahimwalla, K. G. Yager, J. Mamiya, et al., "Azobenzene Photomechanics: Prospects and Potential Applications," *Polymer Bulletin* 69, no. 8 (2012): 967–1006, https://doi.org/10.1007/s00289-012-0792-0.

71. K. M. Lee, M. L. Smith, H. Koerner, et al., "Flexural–Torsional Oscillation of Glassy Azobenzene Liquid Crystal Polymer Networks,"*Advanced Functional Materials* 21, no. 15 (2011): 2913–2918, https://doi.org/10.1002/adfm.201100333.

72. X. Sun, W. Wang, L. Qiu, et al., Unusual Reversible Photomechanical Actuation in Polymer/Nanotube Composites. *Available at Angewandte Chemie International Edition* 51, no. 34 (2012): 8520–8524, https://doi.org/10.1002/anie.201201975.

73. H. Koshima, K. Takechi, H. Uchimoto, et al., "Photomechanical Bending of Salicylideneaniline Crystals," *Chemical Communications* 47, no. 41 (2011): 11423–11425, https://doi.org/10.1039/C1CC14288G.

74. S. Kobatake, S. Takami, H. Muto, et al., "Rapid and Reversible Shape Changes of Molecular Crystals on Photoirradiation," *Nature* 446, no. 7137 (2007): 778–781, https://doi.org/10.1038/nature05669.

75. J. ter Schiphorst, S. Coleman, J. E. Stumpel, et al., "Molecular Design of Light-Responsive Hydrogels, For in Situ Generation of Fast and Reversible Valves for Microfluidic Applications," *Chemistry of Materials* 27, no. 17 (2015): 5925–5931, https://doi.org/10.1021/acs.chemmater.5b01860.

76. R. O. Al-Kaysi and C. J. Bardeen, "*Reversible Photoinduced Shape Changes of Crystalline Organic Nanorods*, *Advanced Materials* 19, no. 9 (2007): 1276–1280, https://doi.org/10.1002/adma.200602741.

77. K. Dholakia and P. Reece, "Optical Micromanipulation Takes Hold," *Nano Today* 1, no. 1 (2006): 18–27, https://doi.org/10.1016/S1748-0132(06)70019-6.

78. M. Tamura, T. Wada, and H. Ishihara, "Basics of Optical Force," *Journal of Photochemistry and Photobiology C: Photochemistry Reviews* 54 (2023): 100570, https://doi.org/10.1016/j.jphotochemrev.2023.100570.

79. T. J. Kippenberg and K. J. Vahala, "Cavity Optomechanics: Back-Action at the Mesoscale," *Science* 321, no. 5893 (2008): 1172–1176, https://doi.org/10.1126/science.1156032.

80. J. Zhang, K. Liu, P. Wang, et al., "Ultra-Long-Range Optical Pulling with an Optical Nanofibre," *Nature Communications* 16, no. 1 (2025): 7424, https://doi.org/10.1038/s41467-025-62536-w.

81. S. Chu, "Laser Manipulation of Atoms and Particles," *Science* 253, no. 5022 (1991): 861–866, https://doi.org/10.1126/science.253.5022.861.

82. K. Zinoviev, C. Dominguez, J. A. Plaza, et al., "Optical Waveguide Cantilever Actuated by Light," *Applied Physics Letters* 92, no. 1 (2008): 011908, https://doi.org/10.1063/1.2830818.

83. M. Li, W. H. P. Pernice, C. Xiong, et al., "Harnessing Optical Forces in Integrated Photonic Circuits," *Nature* 456, no. 7221 (2008): 480–484, https://doi.org/10.1038/nature07545.

84. J. Dorosz, R. S. Romaniuk, M. Chruściel, et al., "Technology of a Photopolymer Microtip as an Optical Fiber Sensor's Transducer," *Proc. SPIE* 10325, Optical Fibers and Their Applications 2017 (2017): 103250E, https://doi.org/10.1117/12.2271037.

85. J. C. Williams and H. Chandrahalim, "Nonlinear Damping as the Fourth Dimension in Optical Fiber Anemometry," *Advanced Sensor Research* 4, no. 1 (2025): 2400080, https://doi.org/10.1002/adsr.202400080.

86. H. Zhao, K. O'Brien, S. Li, et al., "Optoelectronically Innervated Soft Prosthetic Hand via Stretchable Optical Waveguides," *Science Robotics* 1, no. 1 (2016): eaai7529, https://doi.org/10.1126/scirobotics.aai7529.

87. J. C. Knight and P. S. J. Russell, "New Ways to Guide Light," *Science* 296, no. 5566 (2002): 276–277, https://doi.org/10.1126/science.1070033.

88. A. Leber, B. Cholst, J. Sandt, et al., "*Stretchable Thermoplastic Elastomer Optical Fibers for Sensing of Extreme Deformations.*," *Advanced Functional Materials* 29, no. 5 (2019): 1802629, https://doi.org/10.1002/adfm.201802629.

89. Y. Zhou, A. W. Hauser, N. P. Bende, et al., "*Waveguiding Microactuators Based on a Photothermally Responsive Nanocomposite Hydrogel.*,"*Advanced Functional Materials* 26, no. 30 (2016): 5447–5452, https://doi.org/10.1002/adfm.201601569.

90. A. S. Kuenstler, H. Kim, and R. C. Hayward, "Liquid Crystal Elastomer Waveguide Actuators," *Advanced Materials* 31, no. 24 (2019): 1901216, https://doi.org/10.1002/adma.201901216.

91. J. Xiao, T. Zhou, N. Yao, et al., "Optical Fibre Taper-Enabled Waveguide Photoactuators," *Nature Communications* 13, no. 1 (2022): 363, https://doi.org/10.1038/s41467-022-28021-4.

92. Y. He, H. Liang, M. Chen, et al., "Optical Fiber Waveguiding Soft Photoactuators Exhibiting Giant Reversible Shape Change," *Advanced Optical Materials* 9, no. 21 (2021): 2101132, https://doi.org/10.1002/adom.202101132.

93. N. Li, H. Liu, J. Luo, et al., "*Scalable Coaxial Extrusion of Liquid Crystal Elastomer Optical Fiber Enabling Intrinsic Photomechanical Waveguiding-Actuation Synergy*," *Advanced Optical Materials*13, no. 25 (2025): e00993, https://doi.org/10.1002/adom.202500993.

94. H. Liu, Y. He, J. Luo, et al., "Multimodal Actuation and Precise Control in Liquid Crystal Elastomer Optical Fiber Artificial Muscles," *Advanced Materials* (2025): e05776, https://doi.org/10.1002/adma.202505776.

95. L. Tong, "Micro/Nanofibre Optical Sensors: Challenges and Prospects," *Sensors* 18, no. 3 (2018): 903, https://doi.org/10.3390/s18030903.

96. J. H. Chen, D. R. Li, and F. Xu, "Optical Microfiber Sensors: Sensing Mechanisms, and Recent Advances," *Journal of Lightwave Technology* 37, no. 11 (2019): 2577–2589, https://doi.org/10.1109/JLT.2018.2877434.

97. B. O. Guan and Y. Huang, "Interface Sensitized Optical Microfiber Biosensors," *Journal of Lightwave Technology* 37, no. 11 (2019): 2616–2622, https://doi.org/10.1109/JLT.2018.2889324.

98. Y. Li, Z. Xu, S. Tan, et al., "Recent Advances in Microfiber Sensors for Highly Sensitive Biochemical Detection," *Journal of Physics D: Applied Physics* 52, no. 49 (2019): 493002, https://doi.org/10.1088/1361-6463/ab3d4e.

99. Y. Zhen, S. Ma, J. Zheng, et al., "*Waveguide Photoactuator-Enabled Underwater Microgripper* [*Invited*]," *Optical Materials Express* 15, no. 8 (2025): 2026–2036, https://doi.org/10.1364/OME.570820.

100. Y. Meng, Y. Chen, L. Lu, et al., Optical Meta-Waveguides for Integrated Photonics and beyond," *Light: Science & Applications* 10 (2021): 235, https://doi.org/10.1038/s41377-021-00655-x.

101. S. Y. Siew, B. Li, F. Gao, et al., "Review of Silicon Photonics Technology and Platform Development," *Journal of Lightwave Technology* 39, no. 13 (2021): 4374–4389, https://doi.org/10.1109/JLT.2021.3066203.

102. M. W. Pruessner, T. H. Stievater, M. S. et al., "Thermo-Optic Tuning and Switching in SOI Waveguide Fabry-Perot Microcavities," *Optics Express* 15, no. 12 (2007): 7557–7563, https://doi.org/10.1364/OE.15.007557.

103. J. Zheng, Z. Fang, C. Wu, et al., "Nonvolatile Electrically Reconfigurable Integrated Photonic Switch Enabled by a Silicon PIN Diode Heater," *Advanced Materials* 32, no. 31 (2020): 2001218, https://doi.org/10.1002/adma.202001218.

104. A. Guarino, G. Poberaj, D. Rezzonico, et al., "Electro–optically Tunable Microring Resonators in Lithium Niobate," *Nature Photonics* 1, no. 7 (2007): 407–410, https://doi.org/10.1038/nphoton.2007.93.

105. H. Du, F. S. Chau, and G. Zhou, "Mechanically-Tunable Photonic Devices with On-Chip Integrated MEMS/NEMS Actuators," *Micromachines* 7, no. 4 (2016): 69, https://doi.org/10.3390/mi7040069.

106. H. Tian, J. Liu, B. Dong, et al., "Hybrid Integrated Photonics Using Bulk Acoustic Resonators," *Nature Communications* 11, no. 1 (2020): 3073, https://doi.org/10.1038/s41467-020-16812-6.

107. M. W. Pruessner, D. Park, B. J. Roxworthy, et al., "Loss Reduction in Electromechanically Tunable Microring Cavities," *Optics Letters* 44, no. 13 (2019): 3346–3349, https://doi.org/10.1364/OL.44.003346.

108. K. Wu and M. Tichem, "Post-Release Deformation and Motion Control of Photonic Waveguide Beams by Tuneable Electrothermal Actuators in Thick SiO2," *Micromachines* 9, no. 10 (2018): 496, https://doi.org/10.3390/mi9100496.

109. H. Tian, J. Liu, A. Attanasio, et al., "*Piezoelectric Actuation for Integrated Photonics*," *Advances in Optics and Photonics* 16, no. 4 (2024): 749–867, https://doi.org/10.1364/AOP.529288.

110. M. Huang, "Stress Effects on the Performance of Optical Waveguides," *International Journal of Solids and Structures* 40, no. 7 (2003): 1615–1632, https://doi.org/10.1016/S0020-7683(03)00037-4.

111. S. G. Johnson, M. Ibanescu, M. A. Skorobogatiy, et al., "Perturbation Theory for Maxwell's Equations with Shifting Material Boundaries," *Physical Review E* 65, no. 6 (2002): 066611, https://doi.org/10.1103/PhysRevE.65.066611.

112. S. Gyger, J. Zichi, L. Schweickert, et al., "Reconfigurable Photonics with on-Chip Single-Photon Detectors," *Nature Communications* 12, no. 1 (2021): 1408, https://doi.org/10.1038/s41467-021-21624-3.

113. C. Haffner, A. Joerg, et al., "Nano–opto-Electro-Mechanical Switches Operated at CMOS-Level Voltages," *Science* 366, no. 6467 (2019): 860–864, https://doi.org/10.1126/science.aay8645.

114. P. Edinger, A. Y. Takabayashi, C. Errando-Herranz, et al., "Silicon Photonic Microelectromechanical Phase Shifters for Scalable Programmable Photonics," *Optics Letters* 46, no. 22 (2021): 5671–5674, http://doi.org/10.1364/OL.436288

115. M. Li, W. H. P. Pernice, and H. X. Tang, "Tunable Bipolar Optical Interactions between Guided Lightwaves," *Nature Photonics* 3, no. 8 (2009): 464–468, https://doi.org/10.1038/nphoton.2009.116.

116. F. Tian, G. Zhou, Y. Du, et al., "Energy-Efficient Utilization of Bipolar Optical Forces in Nano-Optomechanical Cavities," *Optics Express* 21, no. 15 (2013): 18398–18407, http://doi.org/10.1364/OE.21.018398.

117. P. B. Deotare, et al., "All Optical Reconfiguration of Optomechanical Filters," *Nature Communications* 3, no. 1 (2012): 846, https://doi.org/10.1038/ncomms1830.

118. J. Rosenberg, Q. Lin, and O. Painter, "Static and Dynamic Wavelength Routing via the Gradient Optical Force," *Nature Photonics* 3, no. 8 (2009): 478–483, https://doi.org/10.1038/nphoton.2009.137.

119. D. Lin, F. Deng, W. Hua, et al., "High-Performance Photon-Driven DC Motor System," *Nature Communications* 15, no. 1 (2024): 9506, https://doi.org/10.1038/s41467-024-53924-9.

120. C. Y. Cheng, C. W. Chen, C. C. Li, et al., "Fiber-Tip Microgripper with Sub-Milliwatt Photoactuation," *Advanced Optical Materials* 13 (2025): 2402565, https://doi.org/10.1002/adom.202402565.

121. O. M. Wani, H. Zeng, and A. Priimagi, "A Light-Driven Artificial Flytrap," *Nature Communications* 8, no. 1 (2017): 15546, https://doi.org/10.1038/ncomms15546.

122. M. Zmyślony, K. Dradrach, J. Haberko, et al., "Optical Pliers: Micrometer-Scale, Light-Driven Tools Grown on Optical Fibers," *Advanced Materials* 32, no. 33 (2020): 2002779, https://doi.org/10.1002/adma.202002779.

123. S. Pevec and D. Donlagic, "Optically Controlled Fiber-Optic Micro-Gripper for Sub-Millimeter Objects," *Optics Letters* 44, no. 9 (2019): 2177–2180, https://doi.org/10.1364/ol.44.002177.

124. Y. Xu, W. Fang, and L. Tong, "Real-Time Control of Micro/Nanofiber Waist Diameter with Ultrahigh Accuracy and Precision," *Optics Express* 25, no. 9 (2017): 10434–10440, https://doi.org/10.1364/OE.25.010434.

125. Y. Kang, J. Gong, Y. Xu, et al., "Ultrahigh-Precision Diameter Control of Nanofiber Using Direct Mode Cutoff Feedback," *IEEE Photonics Technology Letters* 32, no. 5 (2020): 219–222, https://doi.org/10.1109/LPT.2020.2966804.

126. N. Yao, S. Linghu, Y. Xu, et al., "Ultra-Long Subwavelength Micro/Nanofibers With Low Loss," *IEEE Photonics Technology Letters* 32, no. 17 (2020): 1069–1072, https://doi.org/10.1109/LPT.2020.3011719.

127. X. Wu and L. Tong, "Optical Microfibers and Nanofibers," *Nanophotonics* 2, no. 5 (2013): 407–428, https://doi.org/10.1515/nanoph-2013-0033.

128. L. Zhang, F. Gu, J. Lou, et al., "Fast Detection of Humidity with a Subwavelength-Diameter Fiber Taper Coated with Gelatin Film," *Optics Express* 16, no. 17 (2008): 13349–13353, https://doi.org/10.1364/OE.16.013349.

129. L. Zhang, J. Pan, Z. Zhang, et al., Ultrasensitive Skin-Like Wearable Optical Sensors Based on Glass Micro/Nanofibers," *Opto-Electronic Advances* 3, no. 3 (2020): 19002201–19002207, https://doi.org/10.29026/oea.2020.190022.

130. Z. Zhang, T. Cai, Z. Li, et al., "Graphene Readout Silicon-Based Microtube Photodetectors for Encrypted Visible Light Communication," *Advanced Materials* 37, no. 1 (2025): 2413771, https://doi.org/10.1002/adma.202413771.

131. Y. Otani, F. Janabi-Sharifi, Y. Hirai, et al., "Light-Driven Micromanipulator and Its Application for 3D Fabrications," *Proc. SPIE* 6374, Optomechatronic Actuators Manipulation, and Systems Control (2006): 63740N, https://doi.org/10.1117/12.689277.

132. H. Cai, K. J. Xu, A. Q. Liu, et al., "Nano-Opto-Mechanical Actuator Driven by Gradient Optical Force," *Applied Physics Letters* 100, no. 1 (2012): 013108, https://doi.org/10.1063/1.3673854.

133. P. Shi, C. Chen, Z. Wang, et al., "Air Plastron–enabled Heat Management for Enhanced Photothermal Actuation in Underwater Soft Robots," *Science Advances* 11, no. 33 (2025): eadx7189, https://doi.org/10.1126/sciadv.adx7189.